Importance of different parameterization changes for the updated dust cycle modelling in the Community Atmosphere Model (version 6.1)

5   Longlei Li[1], Natalie M Mahowald[1], Jasper F Kok[2], Xiaohong Liu[3], Mingxuan Wu[4], Danny M. Leung[2], Douglas S Hamilton[1], Louisa K. Emmons[5] Yue Huang[2,7,8], Jun Meng[2], Neil Sexton[1], and Jessica Wan[6]

[1]Department of Earth and Atmospheric Sciences, Cornell University, Ithaca, NY, United States
[2]Atmospheric and Oceanic Sciences, University of California, Los Angeles, CA, United States
[3]Department of Atmospheric Sciences, Texas A&M University, College Station, TX, United States
10 [4]Atmospheric Sciences and Global Change Division, Pacific Northwest National Laboratory, Richland, WA, United States
[5]Atmospheric Chemistry Observations and Modeling Laboratory, National Center for Atmospheric Research, Boulder, CO, United States
[6]Scripps Institution of Oceanography, University of California San Diego, La Jolla, CA, USA
[7]Earth Institute, Columbia University, New York, NY 10025, USA
15 [8]NASA Goddard Institute for Space Studies, New York, NY 10025, USA

Correspondence to: Longlei Li (ll859@cornell.edu)

Abstract. The Community Earth System Model (CESM; version 2.1) simulates the lifecycle (emission, transport, and
20 deposition) of mineral dust and its interactions with physio-chemical components to quantify the impacts of dust on climate and the Earth system. The accuracy of such quantifications relies on how well dust-related processes are represented in the model. Here we update the parameterizations for the dust module, including those on the dust emission scheme, the aerosol dry deposition scheme, the size distribution of transported dust, and the treatment of dust particle shape. Multiple simulations were undertaken to evaluate the model performance against diverse observations, and to understand how each update alters
25 the modeled dust cycle and the simulated dust direct radiative effect. The model-observation comparisons suggest that substantially improved model representations of the dust cycle are achieved primarily through the new more physically-based dust emission scheme. In comparison, the other modifications except the size distribution of dust in the coarse mode induced small changes to the modeled dust cycle and model-observation comparisons. We highlight which changes introduced here are important for which regions, shedding light on further dust model developments required for more
30 accurately estimating interactions between dust and climate.

1 Introduction

Mineral dust accounts for most aerosol mass in the Earth's atmosphere and plays an important role in different aspects of the coupled Earth-Human-Climate system. For example, dust modifies the radiative budget and atmospheric dynamics via direct, semi-direct, and indirect interactions with radiation (Sokolik and Toon, 1996; Miller and Tegen, 1999; Pérez et al.,

35 2006) and clouds (DeMott et al., 2003; Rosenfeld et al., 2001; Shi and Liu, 2019). In addition, the deposition of mineral dust perturbs the energy budget by darkening snow and glacial ice sheets directly due to the relatively darker color of dust particles (Skiles et al., 2018; Sarangi et al., 2020) and indirectly by providing nutrients (e.g., phosphorus) to snow algae (Mccutcheon et al., 2021). Dust deposited onto land and ocean can also affect the biogeochemistry by adding nutrients (iron and phosphorus) and/or pollutants to ecosystems (Martin et al., 1990; Swap et al., 1992; Shinn et al., 2000; Tie and Cao,

40 2009; Mahowald, 2011; Mahowald et al., 2017, 2010; Hamilton et al., 2020).

To quantify the climate and biogeochemical impacts of dust, accurately reproducing the dust cycle (e.g., emission, transport, deposition, etc.) with models is required. However, previous studies have shown substantial differences between the modeled dust cycle and observations (e.g., surface dust concentration, and dust deposition) (Albani et al., 2014; Wu et al.,

45 2020a). These uncertainties in the dust cycle modeling, as well as uncertainties in optical properties due to dust size and mineral composition suggest a large uncertainty in estimating the dust direct radiative effect (Kok et al., 2017; Li et al, 2021).

The difficulty in modeling dust results primarily from a limited understanding of the processes that control the emission,

50 aging, and removal of dust during transport (Sokolik et al., 2001). Past studies have documented a nonlinear response of dust emission to the soil surface state and meteorological fields (Kok et al., 2012), strong regional variation of the erodible soil composition (Claquin et al., 1999; Journet et al., 2014), complex chemical and physical aging of dust during transport (Cwiertny et al., 2008; Usher et al., 2003) at varied time and spatial scales, a wide range of dust particle size (Mahowald et al., 2014), and irregular shape of dust aerosol particles (Reid et al., 2003a; Wang et al., 2015). These complexities impose a

55 great challenge to parameterizing dust-related processes (e.g., dust emissions and dust deposition) and thus to accurately simulating the dust cycle in climate models. In addition, in situ or station-based measurements of dust aerosols are highly limited at both temporal and spatial scales, which makes representation of those measurements challenging, especially considering the episodic character of dust events (Mahowald et al., 2009). As such, the modeling community is still moving toward better parametrizing the different phases of the dust cycle.

60

To account for regional variations in dust composition and the resultant dust optical properties in estimating the dust direct radiative effect, several common and radiatively important minerals found in dust from major dust sources were introduced to the Community Atmosphere Model versions 4 (CAM4) and 5 (CAM5) (Scanza et al., 2015) and migrated to CAM6.1 (Li et al., 2021), which are the atmosphere components of the Community Earth System Model (CESM: version 1 and 2,

65 respectively). Including the ability to resolve dust speciation along with the addition of an atmospheric iron cycle module (Scanza et al., 2018; Hamilton et al., 2019) facilitates the study of dust impacts on biogeochemical cycles (Hamilton et al., 2020).

This paper describes several updates to the dust representation in CAM6.1 and evaluates whether and for what conditions they improve the dust model comparison to observations. The updates, which are based on up-to-date knowledge of the dust cycle and are thus more physically realistic than the default dust parameterizations in CAM6.1/Community Land Model (version 5; CLM5), include those on

1) dust emissions: Kok et al., (2014a) previously developed a more physically based dust emission scheme for the climate models within the framework of Dust Entrainment And Deposition (DEAD) model (Zender et al., 2003). This scheme performs well against observations in CESM-CAM4 (Kok et al., 2014b) without the aid of an empirical geomorphic dust source function that the current default model CAM6.1 requires (Albani et al., 2014);

2) dry deposition: Particle deposition over smooth and non-vegetated surfaces was less influenced by the interception loss mechanism than over the other surfaces such as grassland. Since the current dry deposition scheme (Zhang et al., 2001; Z01 hereafter) is developed based on measurements over those surfaces, it underemphasizes the interception loss mechanism. The use of the Z01 in the current default CESM2 is, thus, very likely overestimating the dry deposition velocity of fine-sized aerosols (diameter < 1.0 μm; referring to the geometric diameter herein unless stated otherwise) and slightly underestimating that of coarse-sized aerosols (diameter > 5.0μm) (Wu et al., 2018), especially over non-vegetated surfaces (Petroff and Zhang et al., 2010). To mediate this overestimation a future official version of CESM will replace Z01 with the updated scheme (Petroff and Zhang et al., 2010) (PZ10 hereafter);

3) size distribution of dust aerosol particles: one of the changes from CAM5 to CAM6.1 was replacing the size distribution of aerosols in the coarse mode in CAM5 with the one that has a much narrower width in CAM6.1 (Table 1). This change was to accommodate stratospheric aerosols in the coarse mode (e.g., volcanic sulfate) compared to an early officially released version of this model (Mills et al., 2016). A recent model evaluation against satellite retrievals (Wu et al., 2020b) suggest that CESM2-CAM6.1 worsened the dust cycle representation and stands out in simulating the relative importance of wet to dry deposition, compared with the other global climate models or model versions, such as CESM1-CAM5, due partially to the narrow coarse geometric standard deviation;

4) dust particle asphericity: a more recent study (Huang et al., 2020) showed, based on offline calculations, that dust asphericity could lengthen the dust lifetime by ~20%. In addition, we consider the impact of asphericity on optical depth and resulting radiative effect of dust (such as Kok et al., 2017) as has been previously introduced to CAM6.1 (Li et al., 2021).

Table 1. Mode parameters for MAM4 used in CAM5 and CAM6.1 by default: geometric standard deviations (σ or GSD) and geometric mean diameter (GMD) and its ranges. Values in parentheses if present are for CAM6.1. cells without parentheses are kept the same between CAM5 and CAM6.1.

105

Mode	σ (GSD)	GMD (μm)	Lower bound GMD (μm)	Upper bound GMD (μm)
1: Accumulation	1.8(1.6)	0.11	0.054	0.44
2: Aitken	1.6	0.026	0.0087	0.052
3: Coarse	1.8(1.2)	2.0(0.90)	1.0(0.40)	4.0(40)
4: Primary	1.6	0.050	0.010	0.10

We organize the paper as follows: Sect. 2 describes the climate and dust model (Sect. 2.1, 2.2, and 2.3), the modifications we made to the model (Sect. 2.4), and the experiment we conducted (Sect. 2.5) to achieve our purpose. Section 3 presents the observation and semi-observation for model evaluation in current climate. Sect. 4 evaluates the performance of the updated
110   model by comparing simulated dust properties (e.g., surface dust concentrations, deposition fluxes, vertical distribution, and size distribution of transported dust) against observations and semi-observations (Sect. 4.1), quantifies the influence of each modification on those simulated dust properties (Sect. 4.2), documents the influence of those modifications on the estimate of the dust direct radiative effect (Sect. 4.3), and compares these changes in order to recommend which are the most important for other models to consider (Sect. 4.4). Furthermore, we discuss limitations in the model-observation comparison
115   in Sect. 5, recommend future modeling research directions in Sect. 6, and then show the final summarization in Sect. 7.

2 Model descriptions

We used CAM6.1 (Sect. 2.1 and 2.2), embedded within the National Center for Atmospheric Research CESM2.1, to simulate the dust cycle in all the numerical experiments. This section describes dust optical properties and radiation flux diagnostics in CAM6.1 (Sect. 2.3), and our modifications to the base code (Sect. 2.4): the new dust emission scheme and
120   change to the aerosol dry deposition and optics to include dust asphericity. Two sets of simulations with offline dynamics were conducted (Table 2; Sect. 2.5) using bulk (no composition distinguished between particles) and speciated dust. A total of nine experiments were conducted to evaluate the performance of each development that a future version of official model release would likely include on reproducing the dust cycle against that of the current schemes and observations. Five out of the nine experiments quantify how the size treatment for transported dust affects the dust cycle modeling and if those
125   modifications improve the modeled iron solubility. We do not evaluate the model performance on simulating the dust cycle in the preindustrial considering the scarcity of measurements relative to the current climate (Mahowald et al., 2010).

Table 2. Simulations performed in this study for years 2006-2011. Treatment of dust tracer: speciated dust with separate tracers (MINE: mineralogy), or no dust speciation (bulk); the dust emission scheme: Zender et al., (2003a; DEAD) or Kok et al., (2014a; BRIFT); with or

130   without accounting for the lifetime effect of dust asphericity (Asp versus Sph); dry deposition scheme: Zhang et al., (2001; Z01) or Petroff

and Zhang (2010; PZ10); parameters for size distribution taken from the released version of CAM5 (S5) and CAM6.1 (S6); additional test

on dust size distribution (S6σ5) using the coarse-mode σ=1.2 from the released version of CAM6.1 and the rest parameters (e.g.,

boundaries of the geometric mean diameter) from the released version of CAM5; meteorology field nudged toward reanalysis data

(offline) for 2000s climate. CAM6.1 and CAM6.α in bold refer to the default model and proposed new model versions, respectively, with

135   bulk dust.

Exp.	Case names	Dust model	Dry dep.	Asphericity	Emi. scheme	Size
01	**CAM6.1**	Bulk	Z01	No (Sph)	Zender [2003a]	S6
02	NEW_EMIS	Bulk	Z01	No (Sph)	Kok [2014a]	S6
03	NEW_EMIS_SIZE	Bulk	Z01	No (Sph)	Kok [2014a]	S5
04	NEW_EMIS_SIZE_WIDTH	Bulk	Z01	No (Sph)	Kok [2014a]	S6σ5
05	**CAM6.α**	Bulk	PZ10	Yes (Asp)	Kok [2014]	S5
06	MINE_BASE	Mine	Z01	No (Sph)	Zender [2003a]	S5
07	MINE_NEW_EMIS	Mine	Z01	No (Sph)	Kok [2014a]	S5
08	MINE_NEW_EMIS_SHAPE	Mine	Z01	Yes (Asp)	Kok [2014a]	S5
09	CAM6.α_MINE	Mine	PZ10	Yes (Asp)	Kok [2014a]	S5

2.1 Bulk dust modeling

We use the Modal Aerosol Model version 4 (MAM4) in the CESM2.1-CAM6.1 (Liu et al., 2016). We consider both the

default DEAD scheme (Zender et al., 2003) in the current officially released version of CAM6.1 models as well as that of

Kok et al., (2014a) (Sect. 2.4.1). Parameterization of the default dust emissions in DEAD generally follows the dust

140   mobilization mechanism developed by Marticorena and Bergametti (1995) (referred as DEAD hereafter as well). As a

component of CESM2, the CLM initiates dust entrainment once the near-surface friction velocity exceeds the soil threshold

friction velocity, which primarily depends on the physical characteristics of the soil (e.g., soil moisture content, and grain

size distribution) and land cover (Kok et al., 2012; Shao, 2008). The downwind transfer of wind momentum to the surface

soil to produce dust emissions is assumed to be completely prevented by vegetation when the leaf area index (LAI) exceeds a

145   threshold value, 0.3 m^2 m^{-2} (Mahowald et al., 2006a). Below the threshold value, the fraction of a grid cell capable of

releasing dust aerosols is parameterized as an inverse and linear function of LAI (Mahowald et al., 2006a). The inhibition of

soil moisture on dust deflation, and thus dust emission, activates when the near-surface soil gravimetric water content

exceeds a threshold value, determined by the static mass fraction of the clay soil, and is parameterized in the land model

according to a semi-empirical relation (Fécan et al., 1999).

150

The size distribution of the emitted dust is derived using the brittle fragmentation theory developed by Kok (2011b)

distributing 0.1%, 1.0%, and 98.9% percentage of dust mass into Aitken, accumulation, and coarse modes, respectively. This

theory is independent of the friction velocity upon dust emissions (Kok, 2011a), and has been shown to improve the dust

representation in CAM4 relative to the other emitted dust size distribution that CAM4 had previously employed (Albani et

155   al., 2014; Mahowald et al., 2014).

CAM6.1 simulates the advection, deposition, and other aerosol microphysics (e.g., coagulation and nucleation) of aerosols during transport via Module Aerosol Model (version 4: MAM4) using four log-normal size modes (Liu et al., 2016): accumulation (containing sulfate, secondary organic matter, primary organic matter, black carbon, sea salt, and soil dust),

160   Aitken (containing dust, sulfate, sea salt, and secondary organic matter), coarse (containing dust, sea salt, and sulfate), and a primary carbonaceous mode (primary organic matter and black carbon). Within each mode, aerosol tracers are transported as an internal mixture of the species present, while aerosol species from different modes are externally mixed. Also advected in each of the four modes is the number concentration of aerosol particles (Liu et al., 2016), allowing an effective radius to be calculated and the effect of aerosol-cloud interactions to be diagnosed. The removal of dust aerosols is mainly through dry

165   deposition (see Sect. 2.2) and wet deposition, including in- and below-cloud processes, as detailed in Neale et al. (2010). In the formation of precipitating clouds, dust particles can serve as cloud condensation nuclei (CCN) and/or ice nucleating particles (INPs) and thus can be removed via nucleation scavenging (Zender et al., 2003). In addition, the model accounts for the in-cloud scavenging of dust in the Aitken mode by Brownian diffusion, but neglects the other scavenging processes (Easter et al., 2004), which are relatively slow (Pruppacher and Klett, 1997), such as thermophoresis. Below the cloud, dust

170   particles can be removed by the so-called sub-cloud scavenging. This sub-cloud scavenging of dust aerosols follows a first order loss as the product of the precipitation flux, dust mass mixing ratio, and the scavenging efficiency (Dana and Hales, 1976), for example. The wet deposition rate thus depends on the hygroscopicity of dust (=0.068; Scanza et al., 2015) as CCN/INPs and the prescribed scavenging coefficient (=0.1; Neale et al., 2010), both of which are currently constant with respect to the dust size (and composition for speciated dust) in CAM6.1. This size independency of the scavenging

175   coefficient may be an oversimplification, since measurements suggest that it can vary intensively on an order or two even within a size mode (Wang et al., 1978).

The geometric standard deviation (GSD or σ) of each mode is prescribed and default values for CAM5 and CAM6.1 are given in Table 1, along with the initialization of geometric mean diameter (GMD), based on which the model predicates the

180   GMD online, and their ranges. Note that the current default CAM6.1 employs a narrow coarse-mode size distribution but a broad boundary width (high bound minus low bound), likely resulting in the GMD bounds less in effect, compared to that in CAM5. The narrower set of the coarse-mode size distribution was designed to accommodate for stratospheric aerosols (e.g., volcanic sulfate) (Mills et al., 2016), but was not previously compared to dust aerosol observations in detail.

2.2 Speciated dust aerosol modeling

185   The bulk dust model (Sect. 2.1) has previously been modified to speciate the bulk dust into eight mineral tracers, which allows more detailed optical properties as a function of minerals (Scanza et al., 2015; Li et al., 2021). Using the approach of

Claquin et al. (1999), Li et al. (2021) estimated a mean mineralogical composition in the soil at each model grid cell for the minerals illite, kaolinite, montmorillonite, hematite, quartz, calcite, feldspar, and gypsum (Fig. S2 of Li et al., 2021). These minerals represent the most common classes for clay- (soil grain diameter < 2 μm including the first 5 minerals) and silt-
190 sized (diameter between 2-63 μm including the last 5 minerals) soil categories (Claquin et al., 1999). As detailed in Scanza et al. (2015) and Li et al. (2021), additional modifications include: 1) the mineral components in soil types of Gypsic Xerosols and Yermosols, Gleyic and Orthic Solonchaks and salt flats were normalized to unity; 2) the same amount of hematite in the clay- and silt-sized categories was prescribed with equal and opposite change to the illite percentage; 3) the nearest neighborhood algorithm was applied to fill in the grid cells for dust emission; and 4) the soil mineralogy was
195 converted to that of the dust aerosol following the brittle fragmentation theory (Kok, 2011b), as detailed in Scanza et al. (2015).

The distribution of the mass flux for each mineral into the three emission modes follows that of the bulk dust modeling (Sect. 2.1). The sum of the masses of the 8 considered minerals equals the total bulk dust mass without dust speciation. Each of the
200 mineral aerosols are treated as a separate tracer in the same manner as bulk dust, experiencing advection, deposition, and aerosol microphysics (e.g., coagulation). This study did not consider the large uncertainty in the soil mineral abundance (Li et al., 2021) or the uncertainty associated with other physio-chemical parameterizations (e.g., planetary boundary layer, cloud processing, or the heterogeneous reactions on the surface of dust aerosol particles), as the focus of this study is on documenting the impact of the new dry deposition scheme, dust asphericity, and the different emission schemes on the
205 simulated dust cycle.

2.3 Dust optical properties and radiation flux diagnostic

We show results of the direct radiative effect calculations from two code versions: one with the bulk dust and the other with speciated dust. Aerosol optical properties (e.g., single scattering albedo, asymmetry factor) of the internal mixture in an aerosol mode are parameterized based upon the complex refractive index (CRI) of the mixture, which is calculated as the
210 volume-weighted CRI of each component, including water (Ghan and Zaveri, 2007) in that mode. The wet size due to growth of aerosol particles by adsorbing water vapor follows the κ-Kohler theory with a time-invariant hygroscopicity for each aerosol species (Petters and Kreidenwei, 2007). CAM6.1 computes the net radiative flux based on the radiation fluxes diagnosed for each model layer at 14 shortwave and 16 longwave spectral bands per model hour. The direct radiative effect by dust aerosols is then determined by calculating the difference of the net radiative flux with and without dust at the top of
215 the atmosphere under all-sky conditions (here and hereafter unless stated otherwise). This study does not consider the indirect radiative effect which is subject to substantially larger uncertainty due to the complexity involved in cloud microphysics (IPCC, 2021). For the speciated dust, we use the optical properties of the eight minerals, as described in Scanza et al. (2015).

2.4 Changes to the CAM6.1/CLM5 source code

220 The model developments introduced in this section are closely related to the three major components of the dust cycle (emission, vertical transport, and removal mechanism) and the radiative effects. Specifically, we incorporate into CAM6.1 a relatively new dust emission scheme originally developed by Kok et al., (2014a, b), a dry deposition scheme developed by Petroff and Zhang (2010) and incorporated in CAM5 by Wu et al., (2018), and the influence of dust non-spherical shape on the calculated mass extinction efficiency and removal rate of dust aerosol particles (Huang et al., 2020).

2.4.1 Dust emission schemes

225 As part of the DEAD scheme (Zender et al. 2003a), dust sources are strongly associated with the erodible soils (Ginoux et al., 2001). These source regions are parameterized using information contained in the time invariant geomorphology map (Zender et al., 2003) which was optimized (Albani et al., 2014) to match the observed dust optical depth (DOD). Kok et al. (2014a) developed a new dust emission scheme for climate models based on the brittle fragmentation theory (Kok, 2011b; referred to as BRIFT hereafter), which avoided the use of such a static soil erodibility map while improving the accuracy of

230 dust cycle modeling (Kok et al., 2014b); although even dust modeling with BRIFT can be improved if optimized against observations (Kok et al., 2021). Improvements are likely achieved because, compared to that in DEAD, the dust emission in BRIFT tends to be more sensitive to the soil's threshold friction velocity and thus to the surface physical conditions when soil becomes more erodible, owing to the introduced dust emission coefficient (Kok et al., 2014a) and the new method of

235 calculating the threshold gravimetric water content in the top soil layer (see Eq. 4 of Kok et al., 2014b). Descriptions of the DEAD and BRIFT dust emission schemes are detailed in Zender et al., (2003a) and Kok et al., (2014ab), respectively.

2.4.2 Dry deposition schemes

As is typical among aerosols dry deposition resistance models, CAM6.1 includes parameterizations of gravitational settling, aerodynamic and surface resistance. The surface resistance, which dominates over aerodynamic resistance under turbulent

240 conditions, consists of three processes: two applicable to all land types (Brownian diffusion and impaction), and one only to non-smooth surfaces (interception). All the three processes are a function of aerosol size through empirical coefficients constrained by matching the modeled dry deposition velocity with field and laboratory measurements. With more observations available to constraint these coefficients, the default dry deposition scheme (Z01) used in CAM6.1 was found to greatly overestimate dry deposition rates for fine particles (diameter < 1 µm: Aitken and accumulation mode) and slightly

245 underestimate (relative to the large change with fine particles) the rates for coarse particles (diameter around 1 or 2 µm) (Petroff and Zhang, 2010; Wu et al., 2018; Farmer et al., 2020).

The new scheme (PZ10) also includes the effect of different physical processes (thermophoresis, diffusiophoresis, and electricity) occurring between water, ice, and snow surfaces and the air immediately above them, which can result in a

250   downward flux of particles (the so-called phoretic effect; Petroff et al., 2008). PZ10 accounts for such effects of thermophoresis and diffusiophoresis for particle deposition over the three surface types with reduced complexity by assigning constant values of 5×10^{-5} m s^{-1} to water and 2×10^{-4} m s^{-1} to ice and snow surfaces, which allows the scheme to better reproduce the available measurements than Z01 (Petroff and Zhang, 2010). This constant is set to zero for all other surface types. The phoretic effect tends to dominate deposition of fine particles over Brownian diffusion under low wind

255   conditions (friction velocity less than ~ 11 cm s^{-1}). Because of the reduced Brownian diffusion efficiency compared to Z01, PZ10 corrects the high bias seen in Z01 for the deposition of fine particles (Emerson et al., 2020; Petroff and Zhang, 2010; Wu et al., 2018).

2.4.3 Dust asphericity

To account for the influence of dust asphericity on the gravitational settling velocity, we first calculated the asphericity

260   factor γ (defined as the ratio of the gravitational settling velocity of aspherical dust to that of spherical dust) offline based on observed dust shape parameters previously compiled by Huang et al. (2020). We then revised the velocity calculated in the model for dust aerosols only by multiplying it by γ, the global map of which was obtained offline and is shown in Fig. S1, according to Huang et al. (2020). See Supp. "Calculating the asphericity factor" for details.

2.5 Experiment design

265   Table 2 lists the two sets of simulations designed for the present study. The first set of simulations (EXP01-05) utilizes the year 2000 climate with offline dynamics and the officially released model version (CAM6.1) which represents dust as a single bulk composition (termed bulk dust runs hereafter). The second set of simulations (EXP06-09) is the same as the first except that EXP06-09 use the model with dust consisting of eight separate dust mineral tracers (Sect. 2.2).

270   We separately compared the performance of PZ10 to Z01, aspherical to spherical dust, and BRIFT to DEAD on the simulated dust cycle and quantified influence of those modifications on the climatic-effect estimate using the second set of simulations only, as the results are similarly present in this and the first set of simulations. In these two sets of simulations (EXP01-05 and EXP06-09), the CAM6.1 is configured as a stand-alone model where the atmosphere is coupled to active land and sea ice models, and to a data ocean and slab glacier models. Each simulation in these sets was performed at the

275   spatial resolution of $1.25° \times 0.9° \times 56$ (longitude by latitude by vertical layers) using a data ocean for years 2006-2011, with the simulated data for the last five years used for analysis. In addition, the meteorology field (horizontal wind, air temperature T, and relative humidity) was nudged toward the Modern-Era Retrospective analysis for Research and Applications, Version 2 (MERRA-2) at a 6-hour relaxation time scale. The anthropogenic emissions were taken from the Climate Model Intercomparison Program (CMIP6) inventory for the year 2000 (Eyring et al., 2016).

280

Particularly, the bulk dust simulation, EXP01, was performed using the current default version of the model (CAM6.1), and EXP05 using the newly proposed model version, CAM6-α, with bulk dust. It is worth noting that dust burdens and deposition fluxes would be comparable, if the bulk and speciated dust models have similar DOD. But the dust optical properties (e.g., single scattering albedo) in the bulk and speciated dust simulations differ, resulting in considerably different

285 dust direct radiative effects and direct radiative effect efficiencies. Therefore, we state the difference in the dust DRE and DRE efficiency estimate in Sect. 6, but do not document the comparison of dust loadings/deposition/DOD between the bulk and speciated dust simulations.

In all simulations except EXP01, EXP02, and EXP04, we reverted the mode size distribution in CAM6.1 back to that used in

290 CAM5 (Table 1). In EXP01-02, EXP05, EXP06, and EXP07, we tuned the model following Albani et al., (2014), such that the simulated global mean DOD is ~0.03 at the visible band centered at 0.53 µm (hereafter unless stated otherwise), the best estimate obtained by an integrated analysis of the AERONET-based measurements, bias-corrected satellite-retrievals, and a model ensemble (Ridley et al., 2016). Dust tuning was not applied to EXP03 and EXP04 (bulk dust simulations), in which the dust emission was identical to EXP02, in order to see how changes in the transported dust size distribution affects the

295 DOD calculation. Because of the rough linearity among DOD, DRE, and dust burdens (Liao and Seinfeld, 1998; Mahowald et al., 2006b), when comparing surface dust concentrations, dust loadings, and deposition fluxes, we rescaled each of them using the same factor to achieve the DOD ~0.03. For the other cases (EXP08 and EXP09), as will be seen, the global mean DOD only changes slightly within the uncertainty range (0.025-0.035; Ridley et al., 2016). The model retuning is, thus, not required. It's also worth noting that EXP02-05 and EXP06-09 (using as in Kok et al., 2014b) used different methods to

300 calculate the threshold gravimetric water content (see the Supplement for how it is calculated) above which the impression of dust emission due to soil moisture occurs: the former used the default method in CAM6.1-CLM5, the parameterization of Fécan et al. (1998) with the tuning parameter of inverse clay fraction, while the latter used identical parameterization but with unity tuning parameter as in Kok et al. (2014b).

3 Observational datasets for model evaluations

305 Table 3 summarizes available datasets used to evaluate the model performance, detailed descriptions about each datum, and how they are used in the model-data comparison (see supplement for data descriptions: "Descriptions of the data used in the model-observation comparison"; refer to the references for further details about the data).

Table 3. Major observations/retrievals used for model evaluations.

Dust properties	Representative locations	Platform/Instruments	Levels	Time periods	References	Comments

Dust optical depth	Filtered AERONET sites (see Fig. 1a of this study)	Sun photometers	All height levels	2003-2013	Albani et al. (2014)	1) Data quality control; 2) Months selected containing data for at least 10 days; 3) Years selected have a full 12-months coverage; 4) non-dust aerosols filtered out based on the Ångström exponent and single scattering albedo
	Regional averages	Multiple satellite platforms and models	All height levels	2004-2008	Ridley et al. (2016)	Seasonal value obtained by combining four global climate models with multiple satellite aerosol products that were bias corrected using station-based AERONET data
	Terra/Aqua tracks; Regional averages	MODIS	All height levels	2003-2015	Pu et al. (2020)	1) Non-dust aerosols filtered out based on AE and single scattering albedo; 2) An empirical function that relates DOD to AOD and the Ångström exponent
Surface mass concentrations	See Fig. 1d of this study	High-volume filter collectors	Near ground surface	1991-1994	Prospero and Nees (1986) Prospero and Savoie (1989)	This study uses both monthly data and period averaged climatology
Surface deposition fluxes	See Fig. 1g of this study	Sampling filters	At and/or near ground surface	See references	Tegen et al. (2002); Ginoux et al. (2001); Lawrence and Neff (2009); Mahowald et al. (2009)	Data compiled by Albani et al. (2014) and has been processed to get the mass fraction of dust below 10 µm based on reported size parameters, such as geometric standard deviation; see Albani et al. (2014) for details
Wet deposition percentage	Ten sites; see Table 5 of this study (1st column)	See references	At and/or near ground surface	See references	R.Arimoto et al. (1985); Uematsu et al. (1985); Arimoto et al. (1990); Hillamo et al. (1993); Jickells et al. (1998); Wagenbach et al. (1998); Wolff et al. (2006)	Data compiled by Mahowald et al. (2011b)
Size distribution	AERONET sites	Sun photometers	Near ground surface	2003-2013	Holben et al. (1998); Dubovik et al. (2000)	1) AERONET Level 2.0 Almucantar Retrievals (Version 2); 2) data reported for 22 size bins with bimodal size distribution and ellipsoid shape of aerosol particles (Dubovik et al., 2000); only the super micron fraction of dust in the comparison used, even though AERONET may underestimate the mass of dust between 1-10 µm in diameters (McConnell et al., 2008)

	Near the Canary Islands	See Table 1 of Otto et al. 2007	At flight heights: 2700, 4000, 5500, 7000 m	June-July in 1997	Otto et al. (2007)	Data obtained from Fig. 3 of Adebiyi et al. (2020)
	Along flight tracks between the Canary Islands and Mauritania/Mali near Cabo Verde	See Table 3 (second column) of Ryder et al. 2013 for details	At flight heights between 0-3000 and 0-6000 m	June in 2011	Ryder et al. (2013)	Data obtained from Fig. 3 of Adebiyi et al. (2020)
	DustCOMM/global	Joint observation and models	All height levels	See Adebiyi et al. (2020)	Adebiyi et al. (2020)	Data obtained from Fig. 5a of Adebiyi et al. (2020)
Direct radiative effect efficiency	Sahara Desert [15°–30°N, 10°W–30°E]	Satellite CERES and model	TOA	JJA, 2005-2006	Patadia et al. (2009)	Shortwave (0.3-5 μm); clear sky; AOD from MISR and OMI
	Tropical Atlantic [15°–25°N, 15°–45°W]	Satellite CERES	TOA	JJA/NDJ, 2000-2001	Li et al. (2004)	Shortwave (0.3-5 μm); clear sky
	Tropical Atlantic [10°–30°N, 20°–45°W]	Satellite CERES, and model	TOA	JJA, 2007-2010	Song et al. (2018)	Shortwave; clear sky; modelled AOD with constraints from MODIS/CALIPSO
	Atlantic Ocean [0°–30°N, 10°–60°W]	Satellite CERES	TOA	JJA, 2000-2005	Christopher and Jones (2007)	Shortwave; clear sky; AOD from MODIS
	Mediterranean basin [35.5°N, 12.6°E]	Satellite CERES	TOA	September, 2004-2007	Di Biagio et al. (2010)	Shortwave; clear sky; AOD from MFRSR
	North Africa [15°–35°N, 18°W–40°E]	Satellite CERES	TOA	September, 2000	Zhang and Christopher (2003)	Longwave (5-200 μm); clear sky; AOD from MODIS/MISR
	West Africa [16°–28°N, 16°–4°W]	Satellite SEVIRI and GERB	TOA	JJA, 2006	Brindley and Russell (2009)	Longwave; clear sky; AOD from AERONET and MISR
	Niger-Chad [15°–20°N, 15°–22°E]	Satellite SEVIRI and GERB	TOA	JJA, 2006	Brindley and Russell (2009)	Longwave; clear sky; AOD from AERONET and MISR
	Sudan [15°–22°N, 22°–36°E]	Satellite SEVIRI and GERB	TOA	JJA, 2006	Brindley and Russell (2009)	Longwave; clear sky; AOD from AERONET and MISR
	Egypt/Israel [23°–32°N, 23°–35°E]	SEVIRI and GERB	TOA	JJA, 2006	Brindley and Russell (2009)	Longwave; clear sky; AOD from AERONET and MISR
	North Libya [27°–33°N, 15°–25°E]	Satellite SEVIRI and GERB	TOA	JJA, 2006	Brindley and Russell (2009)	Longwave; clear sky; AOD from AERONET and MISR
	South Libya [23°–27°N,15°–25°E]	Satellite SEVIRI and GERB	TOA	JJA, 2006	Brindley and Russell (2009)	Longwave; clear sky; AOD from AERONET and MISR
	Sahara Desert [15°–30°N, 10°W– 30°E]	Satellite CERES	TOA	JJA, 2005-2006	Yang et al. (2009)	Longwave; clear sky; AOD from MISR and OMI
	Tropical Atlantic [10°–30°N, 20°–45°W]	Satellite CERES and model	TOA	JJA	Song et al. (2018)	Shortwave; clear sky; modelled AOD with constraints from MODIS/CALIPSO
	Atlantic Ocean [0°–30°N, 10°–60°W)	Satellite CERES	TOA	JJA, 2000-2005	Christopher and Jones (2007)	Longwave; clear sky; AOD from MODIS
	Cape Verde [16.7°N, 22.9°W]	Models	TOA	September, 2006	Hansell et al. (2010)	Longwave; clear sky; AOD from MFRSR, MPL, CALIPSO, and AERI

	Zhangye, China [39°N, 101°E]	Ground-based SMART	TOA	AMJ	Hansell et al. (2012)	Longwave; clear sky; AOD from MFRSR, MPL, CALIPSO, and AERI

310 List of acronyms

AERONET: Aerosol Robotic Network

MODIS: Moderate Resolution Imaging Spectroradiometer

DustCOMM: Dust Constraints from joint Observational-Modelling-experiMental analysis

CALIPSO: Cloud-Aerosol Lidar and Infrared Pathfinder Satellite Observations

315 CALIOP: Cloud-Aerosol Lidar with Orthogonal Polarization

AIRS: Atmospheric Infrared Sounder

CERES: Clouds and the Earth's Radiant Energy System

TOA: top of the atmosphere

AOD: aerosol optical depth

320 MISR: Multi-angle Imaging SpectroRadiometer

OMI: Ozone Monitoring Instrument

MFRSR: MultiFilter RotatingShadowband Radiometer

SEVIRI: Spinning Enhanced Visible and Infrared Imager

GERB: Geostationary Earth Radiation Budget

325 AERI: Atmospheric Emitted Radiance Interferometer

SMART: NASA Goddard's ground-based mobile laboratories

4 Results

Each of the modifications made to CAM6.1 (described in Sect. 2.2) is relevant to the modeled dust cycle, and, thus, relevant to the estimate of dust climatic impacts (e.g., direct radiative effects). The proposed new (CAM6.α) and default model

330 versions (CAM6.1) simulated a similar (Fig. S2a: relative change ~16%; CAM6.α relative to CAM6.1) global mean dust loading of 24 and 29 Tg, respectively, and DOD of 0.032 (Fig. S2c: relative change<1.3%) (Table 4). Comparing to the recent estimates that include very coarse dust which are not included in this model, the dust loadings here are well within the range of 22-30 Tg in Kok et al. (2021) (Table 1 of their study), and are close to the 30 Tg in Adebiyi and Kok (2020). But globally CAM6.α shows 54% more dust deposition than in CAM6.1 (Fig. S2b). The general spatial distributions of the

335 relative change of dust loadings, deposition fluxes, and DOD are similar, though the magnitude of this change differs for some regions (e.g., North Africa, India).

The aforementioned differences between CAM6.α and CAM6.1 could change their performance against the observations, which is detailed in Sect. 4.1. Then in Section 4.2 we show how each of the modifications affect the simulation of the dust

340 surface concentration, dust surface deposition fluxes, dust loadings, size distribution of dust aerosols, and the vertical distribution of dust plumes. Sect. 4.3 presents influence of the modifications on the estimate of dust DRE and DRE efficiency. We compare the relative importance of each modification on the simulated dust loadings, deposition, and on the estimate of the dust DRE in Sect. 4.4.

345   **Table 4.** Simulated annual emission, loading, surface concentration, deposition, lifetime, DRE (all-sky conditions) and DREE (DRE efficiency; all-sky conditions) of dust speciated by mineralogy CAM6S5 and bulk dust CAM6S6 with offline dynamics. The longwave direct radiative effect by dust was augmented by 51% (Dufresne et al., 2002) to account for dust scattering which is not represented in CAM by default. DOD and SSA shown are for the CAM6.1 visible band centered at 0.53 µm. The global mean dust SSA was calculated over model pixels where DOD/total AOD>0.5 as previously did (Scanza et al., 2015; Li et al., 2021). CAM6.α and CAM6.1 in bold

350   represent the proposed new and default model versions, respectively.

Cases	Emissions (Tg a^{-1})	Dust loadings (Tg)	Surf conc. (µg cm^{-3})	Deposition (Tg a^{-1})	Lifetime (days)	DOD	Dust SSA	SW DRE (W m^{-2})	LW DRE (W m^{-2})	Net DRE (W m^{-2})	Net DREE (W m^{-2} τ^{-1})
CAM6.1	2421	29	38	2427	4.3	0.032	0.918	-0.50	0.20	-0.30	-9.4
NEW_EMIS	1606	22	25	1609	4.9	0.030	0.931	-0.66	0.42	-0.24	-8.0
NEW_EMIS_SIZE	1621	11	14	1622	2.4	0.013	N/A	-0.39	0.30	-0.094	-7.2
NEW_EMIS_SIZE_WIDTH	1612	11	14	1613	2.4	0.019	0.936	-0.51	0.31	-0.20	-11
CAM6.α	2891	24	25	2893	3.0	0.030	0.911	-0.45	0.19	-0.26	-8.7
MINE_BASE	4456	27	41	4459	2.2	0.035	0.897	-0.38	0.24	-0.14	-4.0
MINE_NEW_EMIS	2910	25	26	2912	3.1	0.029	0.900	-0.29	0.23	-0.06	-2.1
MINE_NEW_EMIS_SHAPE	2914	26	27	2916	3.2	0.030	0.900	-0.30	0.24	-0.06	-2.0
CAM6.α _MINE	2869	24	25	2871	3.1	0.031	0.896	-0.31	0.24	-0.07	-2.3

4.1 Evaluation of model performance and improvements on the dust cycle modeling

4.1.1 Dust emissions

355   To achieve the global mean DOD of ~0.03, CAM6.α requires a dust emission of 2891 Tg a^{-1} (Table 4), which falls below the estimate of 3400-9100 Tg a^{-1} by Kok et al. (2021; their Table 1) that accounts for dust between 0.1-20 µm in diameter. The dust emission in CAM6.1 is also much lower than their estimate: 2421 Tg a^{-1}, which is, however, higher than the previous estimate (1490 Tg a^{-1}) with the same emission scheme (DEAD) and dust size range (<10 µm) but using the binned method (Zender et al., 2003).

360

There are no dust emission estimates from observations at global scale. We thus infer the model performance on simulating dust emissions using model-data comparisons on the surface dust concentration and deposition flux. However, such an evaluation of emission is probably achievable only when the observation site is close to the dust source. Otherwise, the reasoning would become incorrect, because of probable additional errors from the model representation on processes of dust

365   transport and deposition, and interaction of dust with non-dust aerosols (e.g., sea salt and biomass burning). As will be seen in Sect. 4.1.3 and 4.1.4, in most of the grid cells containing the observational sites in North Africa, the models overestimated the deposition fluxes (Fig. 1g) and the surface dust concentrations (at Bani). This might suggest that the model, with the

current settings and the global tuning toward DOD ~0.03, probably overestimated dust emissions from North African sources, which is also shown in Kok et al. (2021) using an integrated model ensemble and observational constraints.

370

The locally emitted dust from the high-latitude region (> 50º N and < 40º S) in CAM6.α constitutes ~1.6% of the global total emitted dust flux, which is below the estimate of ~5% (2-3% for each hemisphere) derived from field and satellite observations (Bullard et al., 2016; Bullard, 2017). Especially for the northern high-latitude region, where local dust sources may dominate the near surface dust concentrations (Groot Zwaaftink et al., 2016), CAM6.α substantially underestimated its

375 contribution to the global dust (<0.1%). This underestimation is what we expected, since the new scheme is designed to simulate dust emissions in low-latitude regions predominantly from the impact of saltators (Kok et al., 2012) and thus may not well capture the high-latitude dust emissions which occur through different physical processes. In comparison, despite missing dust sources > 60º S (Fig. 2a), CAM6.1 may overestimate the contribution of high-latitude dust emissions to the global dust total (8.0%). We attribute the much higher dust emission in the southern high-latitude region in CAM6.1

380 primarily to the higher emission from the South American sources (i.e., the Patagonian Desert) than in CAM6.α. This much higher dust emission is not due to local dust emissions from the Antarctic, because the local emission in the Antarctic though exists (Delmonte et al., 2013; Meinander et al., 2021; and Fig. 2b), it is weaker in strength (the contribution percentage <0.01%) than Patagonian Deserts (Fig. 2b), and the two models (CAM6.1 and CAM6.α) also simulated a percentage contribution of dust emission from the Antarctic sources comparable to each other. Since both dust emission schemes are far

385 from perfect in reproducing percentage contribution to the global dust emission and thus probably the high-latitude dust loadings, especially in the Arctic (i.e., Fig. 1e of Shi and Liu, 2019) where dust aerosol could impose big impact on polar clouds (Shi et al., 2021), a regional tuning of the local emission in the high-latitude regions is needed to better quantify the dust-cloud and dust-radiation interactions there.

390 **4.1.2 Climatology annual means of dust optical depth, surface concentrations, and deposition fluxes**

Overall, all models reproduced the climatology of DOD from AERONET retrievals, the surface concentration, and deposition within a factor of ten (Fig. 1 and Fig. S3), with the spatial correlation between the models and observations statistically significant at the 95% confidence level based on Student's t test. Analysis of the spatial correlation (Pearson; R) and root mean square error (RMSE except for the surface dust concentration) suggests a substantial and statistically

395 significant improvement in simulating DOD close to source region (Fig. 1c versus Fig. 1b: R=0.63 versus 0.41 for CAM6.α and CAM6.1, respectively, in log space; RMSE=0.30 versus 0.41 in log space). Note we obtained the RMSE in log space which removes the dominant influence of stations with high DOD (i.e., sites in North Africa and Middle East). So, the reduced bias is because the new model better captures DOD over North Africa and Australia. Compared to the improvement in DOD, the modifications do not notably better improve modeling the surface dust concentrations (Fig. 1f versus Fig. 1e:

400 R=0.86 versus 0.75 for CAM6.α and CAM6.1, respectively; similar RMSE≈0.70 in both models) and dust deposition (Fig. 1i

and Fig. 1h; R: 0.78 versus 0.69 and RMSE=0.85 versus 0.97). This is because the model's ability to simulate DOD, especially close to source regions, is subject to fewer potential errors than for surface dust concentration and deposition, which also require the model to simulate a correct vertical distribution. Therefore, the model's ability to reproduce DOD close to source region appears to have improved at most of the sites (33 out of a total of 36 sites; especially in Australia as shown in Fig. 1a), but this improvement did not propagate to simulations of the dust surface concentrations (Fig. 1d: improvement at 24 out of a total of 47 sites) and deposition (Fig. 1g: improvement at 62 out of a total of 108 sites).
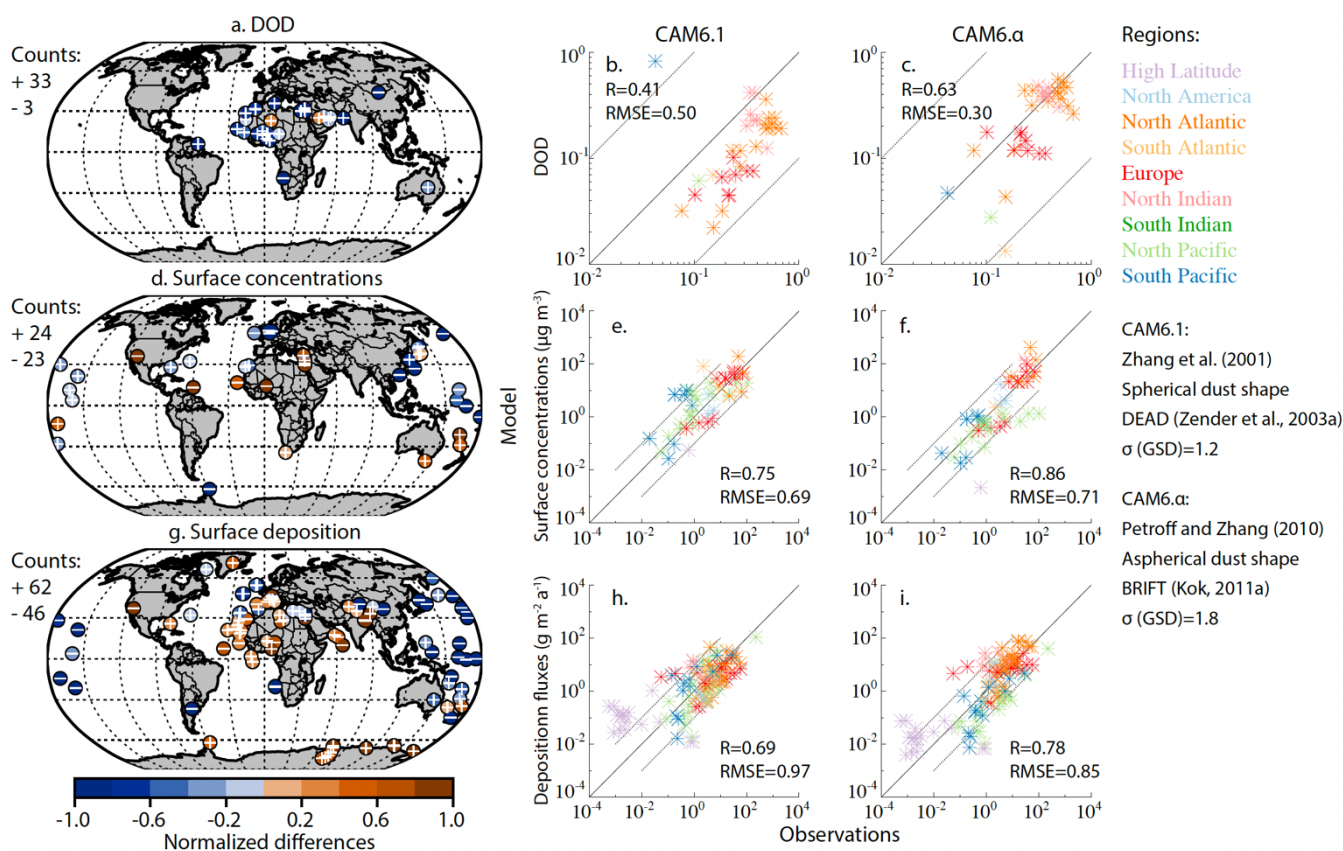
Figure 1. Model-observation (AERONET) comparison for DOD (dust optical depth) at the visible band centered at 0.53 μm (a, b, and c), dust surface concentrations (d, e, and f), and surface deposition fluxes (g, h, and i). Colored dots in a, d, and g show the difference between the proposed new model (CAM6.α) and observations. White symbols indicate the new model CAM6.α improves (plus sign) or worsens (minus sign) the model-observation comparison over that between the default model (CAM6.1) and observations. Numbers listed in a, d, and g are counts of the number of improved or worsen stations. The spatial correlation coefficients between model (CAM6.1: b, e, and h; CAM6.α: c, f, and i) and observations were calculated based on the annual mean values in log space (the log of each model and observational value was taken before calculating the correlation coefficient, since the values span several orders of magnitude except DOD). Dash lines in the scatter plot show 10:1 or 1:10 lines. Fig. S3 shows the scatter plots for some of the other cases, such as MINE_BASE, MINE_NEW_EMIS, and MIINE_NEW_EMIS_SHAPE.
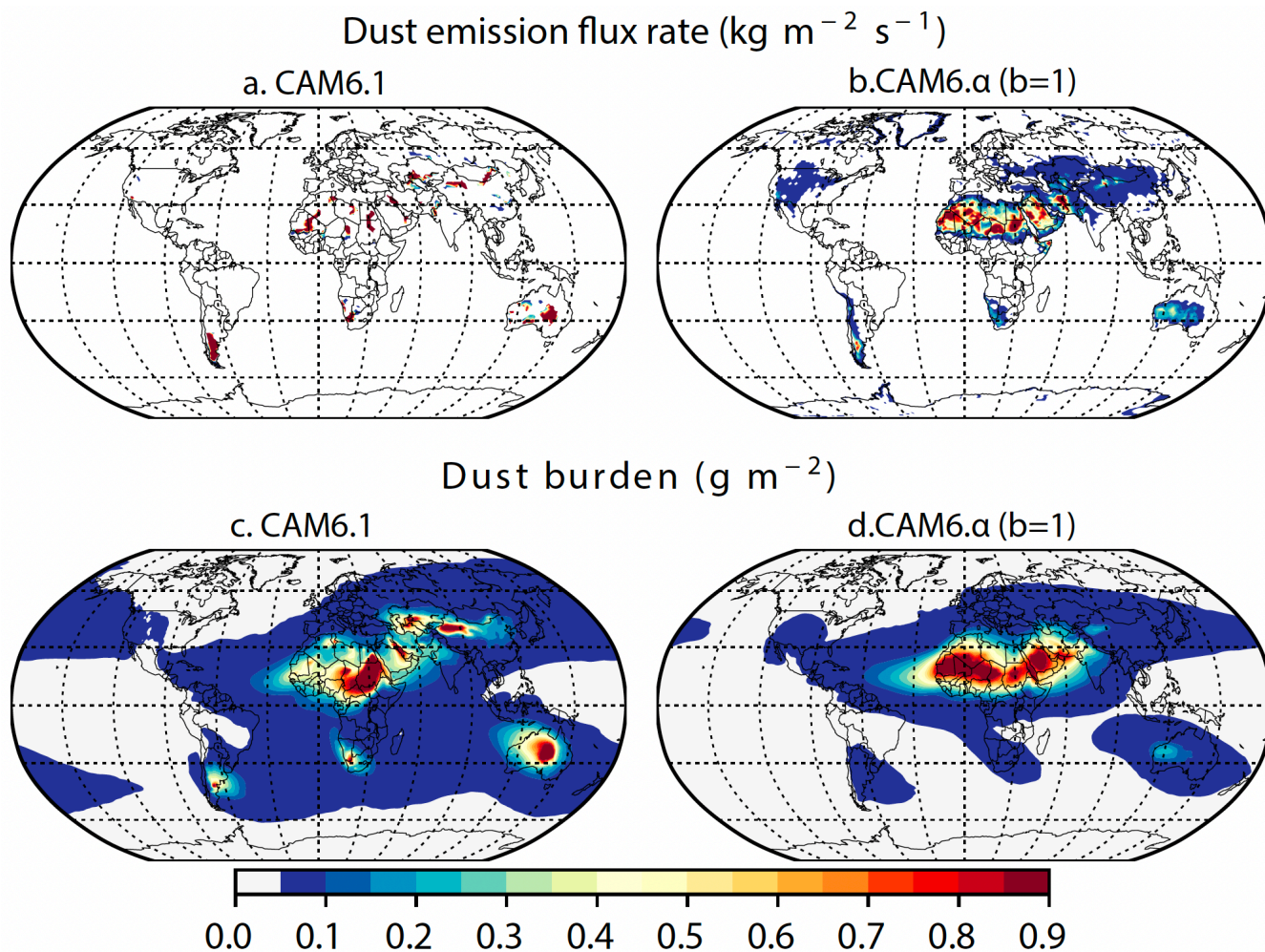
Figure 2. Dust emission flux rate (kg m^{-2} s^{-1}; panels a and b) and dust burdens (panels c and d) simulated in default CAM6.1 (panels a and c; dust emission flux rate rescaled up by 10^9) and new model CAM6.α with the threshold gravimetric water content calculated following Fécan et al. (1999) using unity tuning factor (b=1 in panels b and d; dust emission flux rate rescaled up by 10^8 in panel b).
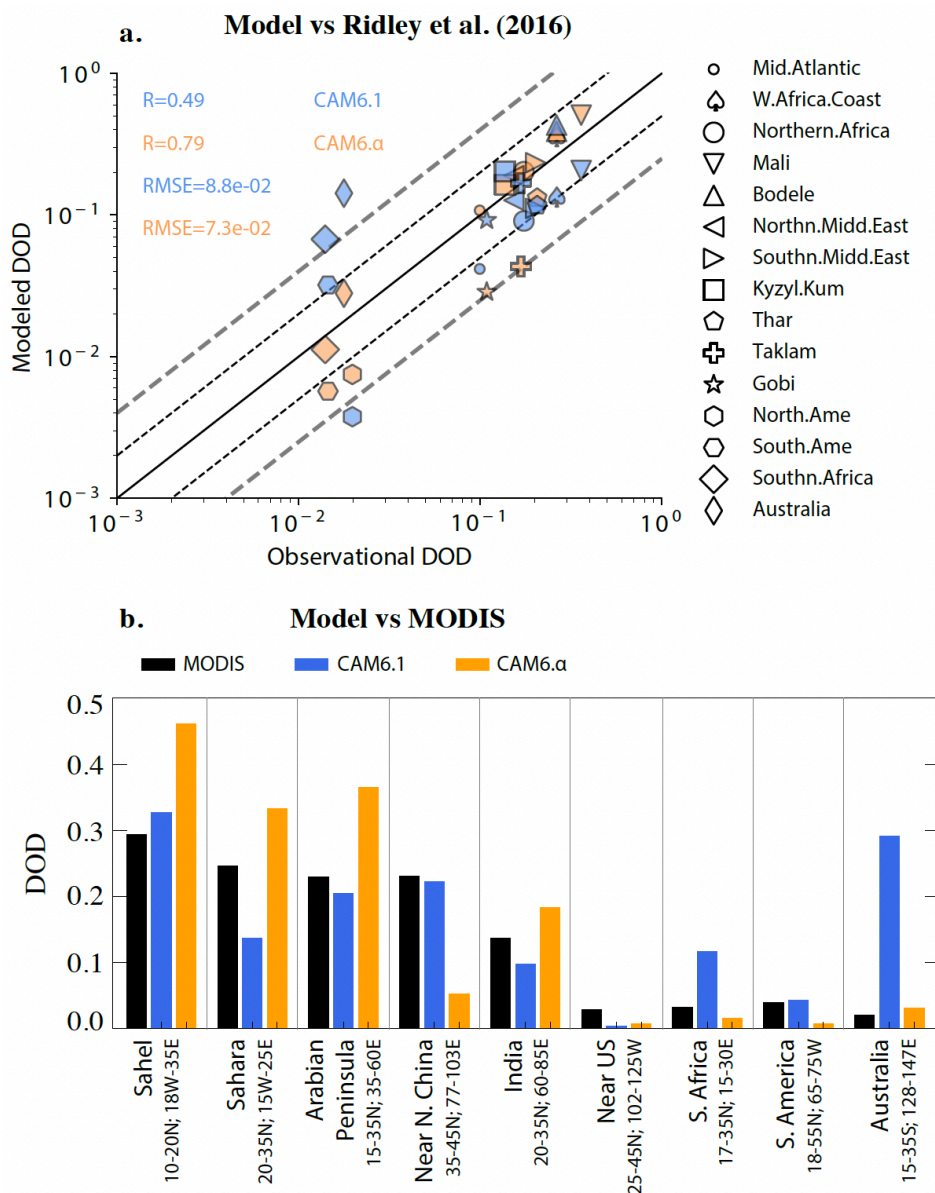
Figure 3. Modeled DOD in CAM6.1 (blue) and CAM6.α (orange) in comparison with that from Ridley et al. (2016) at sub regions as defined in their Fig. 1 and from MODIS retrievals (b) at sub regions (see x-axis labels). Both correlations, shown as the Kendall's τ in panel (a), are statistically significant at the 95% confidence level. Black and grey dash lines in panel (a) represent a factor of 2 and 4 differences.

Improvements are also seen if the climatologic DOD is compared to regional averges of the observationally constrained DOD in Ridley et al. (2016) (Fig. 3a). The new model CAM6.α substantially improved the modeled DOD, increasing the correlation (Kendall's τ coefficient) from 0.49 to 0.79 and reducing RMSE from 0.088 to 0.077, compared to CAM6.1.

Spatially, CAM6.α much better capture the regional DOD averaged over Australia and South Africa, which is consistent to comparison with the regional MODIS DOD (Fig. 3b). Over Taklimakan and Gobi deserts, however, the new model greatly underestimated the regional DOD compared to both estimates from Ridley et al. (2016) (Fig. 3a) and MODIS DOD (Fig. 3b; near northern China), whereas the default CAM6.1 works better, due very likely to the low dust emissions in the source

440   regions in CAM6.α than in CAM6.1 (Fig. 2b versus Fig. 2a). Comparing with both datasets suggests that the new model may overestimate the regional DOD over North Africa and Middle East within a factor of two. Despite the imperfect math on the period between data and model and some other factors (See Sect. 4), this overestimated regional DOD probably results from the retuning method, which provides more credits to dust emission from North Africa and Middle East.

445   The underestimation in the surface dust concentration and overestimation in deposition occurring at several sites (near the El Djouf; near the Antarctic from our model in all cases) is noteworthy. At some sites, such as King George in the Antarctic (62ºS, 58ºW), this phenomenon has been previously revealed by studies with multiple model ensemble mean or individual models, including an earlier version of CAM, model-data integrated study (Kok et al., 2021a), in the results of models other than CAM6.1, such as GFDL Atmospheric Model (version 2) (Li et al., 2008), and in earlier versions of CAM (Albani et al.,

450   2014). We suggest that the phenomenon occurs likely in part due to 1) model errors in simulating dust wet and dry deposition which is substantially larger than in simulating DOD and surface concentrations (Kok et al., 2021b): in addition to errors in and dust emissions, and the parameterization of the dry and wet deposition schemes, MAM4 in CAM6.1 represents dust transport as an internal mixture with other species (e.g., sea salt) in the accumulation and coarse modes (Liu et al., 2016), which may have unduly increased the particle size and hygroscopicity, and, thus, the removal rate (dry and wet) of

455   dust during transport to the sites (i.e., King George); 2) the possible misrepresentation of dust sources in the Southern Hemisphere in the model. With the current emission sources, the increase of the emission rate with BRIFT from Patagonia compared to DEAD slightly mediated the underestimated dust surface concentration at King George. A further increase of the dust emission may help reduce the underestimation of dust deposition in land and the surface concentration at King George, but it would then exacerbate the bias in simulating the surface deposition at that site; 3) the limited observation

460   period which could result in the climatology representative issue, considering the episodic character of dust events. This limitation due to observation period may be particularly important for observed dust in the Southern Hemisphere where the dust quantities tend to be more episodic than in the Northern Hemisphere (Mahowald et al., 2011).
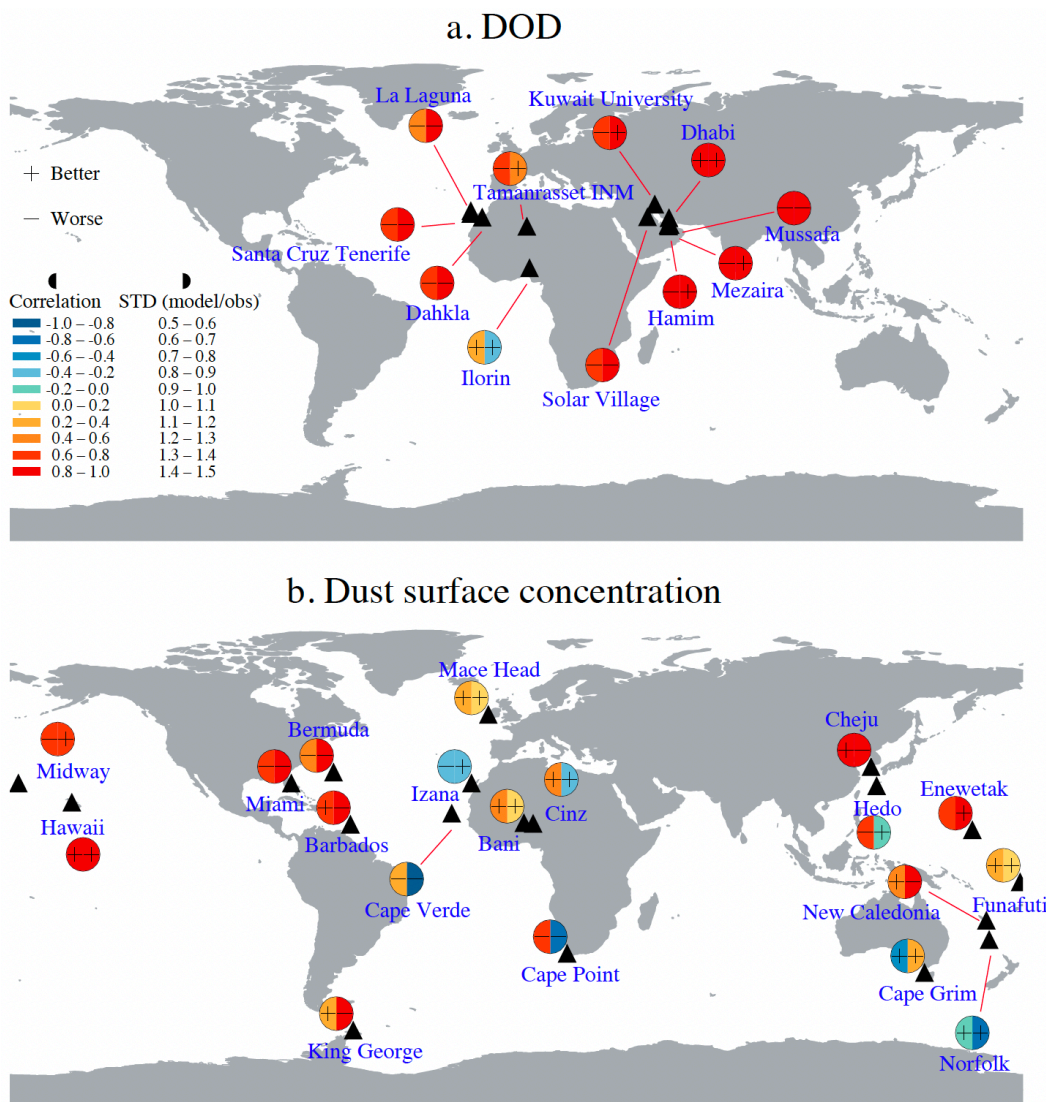
19

Figure 4. Modeling performance for the seasonal cycle of DOD (a) and dust surface concentrations (b) by CAM6.α (new model) against in situ (site names listed in the figure) measurements, relative to the performance of CAM6.1 (default model) against in situ measurements (improvement, degradation, no change indicated by "+", "-", and none characters, respectively). Colored left and right semi-circles represent Kendell's τ coefficient between CAM6.α and observations and the ratio of standard deviation (CAM6.α over observation; each normalized by annual mean values), respectively.

As to the relative importance of dry and wet deposition, we find that the dust wet deposition may dominate the total deposition of dust, especially in the remote oceanic area (Fig. S4a), and thus affects the long-range dust transport. Considering the limited observations on the partitioning of the dust total deposition between dry and wet processes, however, we cannot draw a concrete conclusion that CAM6.1 overestimates the wet dust deposition fluxes (Table 5). With that said, a

recent study has shown that the CMIP6 models overestimate the precipitation frequency, particularly for the light
475   precipitation (0.1-20 mm per day) (Na et al., 2020). It could be the same reason – the unduly simulated precipitation
frequency in CAM6.1 – that explains the overestimated importance of wet deposition, compared to the observations we have
here. Therefore, future model changes on the cloud physics that reduce the light precipitation frequency may help better
simulate the transport of dust aerosols across zones where frequent precipitation occurs (i.e., the ITCZ zone).

480   **Table 5.** Percentage (%) of wet deposition. Observations compiled by Mahowald et al., (2011b) from data at Bermuda (Jickells et al.,
1998), Amsterdam Island, Cape Ferrat, Enewetak Atoll (R.Arimoto et al., 1985), Samoa; New Zealand sites (Arimoto et al., 1990); North
Pacific sites (Uematsu et al., 1985); Greenland Dye 3 (Hillamo et al., 1993), Coastal Antarctica (Wagenbach et al., 1998), and Dome C of
Antarctica (Wolff et al., 2006).

Location	CAM6.1	CAM6.α	MINE_BASE	MINE_NEW_EMIS	CAM6.α_MINE	Observations
Bermuda	92	87	81	85	87	17-70
Amsterdam Island	88	81	78	80	83	35-53
Cape Ferrat	92	86	87	84	86	35
Enewetak Atoll	79	66	58	56	64	83
Samoa	91	86	83	81	85	83
New Zealand	89	87	80	85	88	53
North Pacific[a]	62-90	53-85	46-80	48-80	56-84	75-85
Greenland	82	86	75	86	84	65-80
Coastal Antarctica	96	93	82	87	88	90
Dome C. Antarctica[b]	97	96	88	89	91	20[b]

[a] shown are minimum and maximum of the annual wet percent among the four sites
485   [b] Non sea salt-sulfate

4.1.3 Seasonal cycle of climatology dust optical depth and surface dust concentrations

Dust optical depth

Both CAM6.1 and CAM6.α reasonably reproduced the retrieved seasonal cycle at the selected AERONET sites except Ilorin
490   (Fig. S5), where both models greatly underestimated the observed DOD in winter (Fig. S5b). It is possible that non-dust
aerosols (e.g., black carbon) transported from the South Africa contaminated the observation, leading to an artificially high
DOD during the winter season at that site.

The new model CAM6.α improved both the temporal correlation based on the monthly values and standard deviation,
495   compared to CAM6.1, only at two (Ilorin, and Dhabi) out of a total of the eleven selected AERONET sites where the
measurements cover the whole twelve months in a year (Fig. 4a). Significant improvements on the modeled seasonal cycle
of DOD occurs at Tamanrasset (25ºN, 4ºE). CAM6.α increased the temporal correlation coefficient from 0.42 to 0.82 (Fig.

S5i). Despite the improvement, the new model continued largely overestimating the observed DOD at this site, especially in the peak month June (Fig. S5i), resulting in an overestimated annual mean DOD.

500

Similar results are obtained if the seasonal cycle of DOD is compared to model-data constraints on regional DOD in Ridley et al. (2016) (Fig. S6): spatial correlation analysis on the seasonal mean DOD suggests that the new model CAM6.α substantially improved the modeled DOD in all seasons (Fig. S6) with reduced root-mean-square errors (RMSEs) and higher correlations that are statistically significant (Table S1), compared to simulations using CAM6.1 (i.e., in JJA CAM6.α:

505 R=0.71 and RMSE= 0.085 versus CAM6.1: R=0.48 and RMSE=0.12; Kendall's τ coefficient).

Surface dust concentrations

In terms of temporal correlation and standard deviation for assessing the seasonal cycle, the modifications do not uniformly improve the model performance on reproducing the surface dust concentration (Fig. 4b). Only at seven out of the nineteen sites in total (a reduced number of the total sites, compared to that used in the climatology comparison, due to the removal of

510 sites where there is no full coverage of the measurement over the twelve months in a year) - Bani and Cinz in North Africa, Mace Head in the North Atlantic, Cape Grim in Australia, and Hawaii in the North Pacific (Fig. 4b) - the modifications result in improvements using both metrics. Examining a third metric, the difference between modeled and observed surface concentration in specific months, we have thirteen of the nineteen sites where at least half a year shows improvement. Still, the new model overestimated the surface concentration of dust at many of those thirteen and other sites during most months

515 in the year (Fig. S7-8). This overestimation is particularly pronounced for Cape Verde, likely mainly because of the strong dust emission in western North Africa using BRIFT compared to DEAD. The new model produced significant improvement in terms of all the three metrics at Bani (14ºN, 3ºE; Fig. S8i), increasing the temporal correlation from 0.21 (insignificant at the 95% confidence level) between CAM6.1 and the observation to 0.58 (significant at the same confidence level) between CAM6.α and the observation.

520 **4.1.4 Size distribution of transported dust**

We show the simulated size-resolved dust mass compared to AERONET retrievals and in situ measurements in Fig. S9. In general, the new model CAM6.α with the mode size distribution from CAM5 better reproduced the retrieved atmospheric size distribution than the default CAM6.1 with the size distribution from CAM6.1 over most sites. Only at 2 sites (La Laguna: 28ºN, 17ºW; and Puerto Rico) the mass size distribution from CAM6.α becomes worse than from CAM6.1.

525 Compared to CAM6.α, CAM6.1 tends to carry more dust in mass with the diameter >~5.0 μm, which also overshot AERONET retrievals in that size range (Fig. S9). The bias in CAM6.1 could be even higher for mass of dust >~5.0 μm, considering that AERONET retrievals might have a bias towards fine dust when compared to in situ measurements (McConnell et al., 2008).
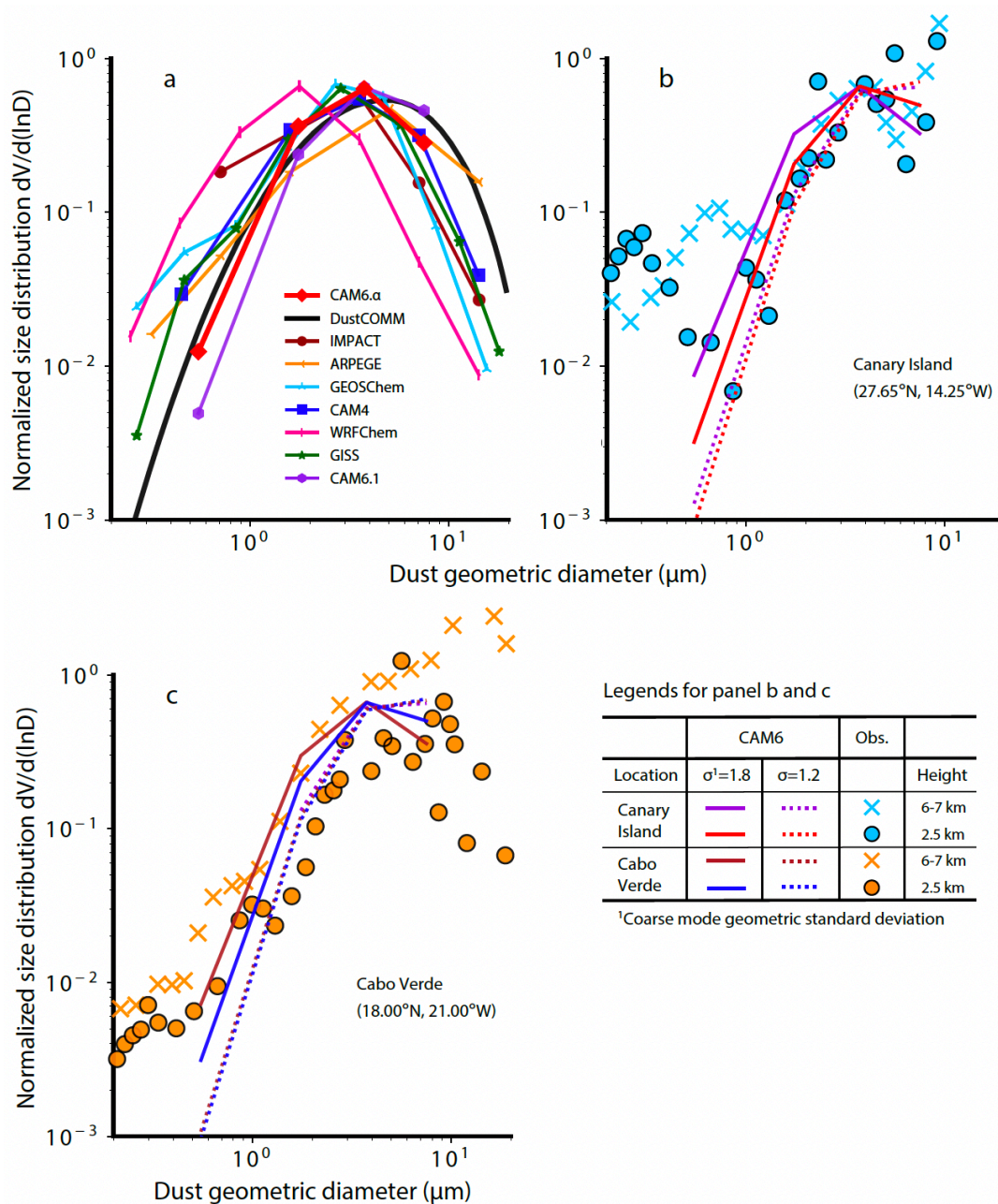
Figure 5. Normalized size distribution of dust between 0.2 and 10 μm diameter in the global average (a), near Canary Island (blue colors in b; dot: 2.5 km; x: 6-7 km; data for June/July 1997 from Otto et al., 2007), and near Cabo Verde (orange colors in c; dot: 2.5 km; x: 6-7 km; data for August 2015 taken from Ryder et al., 2018) and. The default model, CAM6.1: (purple line); the new model, CAM6.α: (red line) (for the abbreviation of other models see Adebiyi et al., 2020); semi-observations: DustCOMM (black line); and other climate models with data taken from Adebiyi et al. (2020). We chose the model layers and grid cells that are closest to the location and atmospheric

535   height, as well as the months, where and when the measurements were made for comparison. See Fig. S10 for the model-observation comparison at other atmospheric levels.

When comparing global mean model results to those from DustCOMM (Adebiyi et al., 2020) (Fig. 5a), generally, CAM6.α better reproduced the atmospheric size distribution (dV/dlnD) than most of the other models (e.g., WRF-Chem: Weather
540   Research Forecasting-Chemistry) in the full size range, and CAM6.1 for dust < 2 μm in diameter (Fig. 5a). Like most climate models shown in Fig. 5a, CAM6.1 tends to underestimate coarse dust with the diameter greater than ~5 μm and the model currently excludes super coarse dust (diameter > 10 μm). The size distribution from CAM6.1 compares well with the DustCOMM result for dust > 2 μm in diameter, but it greatly underestimated the fine dust fraction (diameter < 2 μm) which CAM6.α can better capture.

545

We then evaluated the model's performance in reproducing the size distribution measurements at the high-atmosphere levels (2-5 and 6-7 km) near the Canary Island (Fig. 5b) and Cabo Verde (Fig. 5c) where Ryder et al. (2018) and Otto et al. (2007) for transported dust. Overall, CAM6.α better reproduced the size distribution at the higher atmospheric level (6-7 km) than CAM6.1, but CAM6.α substantially overestimated dust mass at the lower atmospheric level (2-5 km) compared to the
550   measurements where CAM6.1 performed better. As also suggested in the global size distribution comparison, CAM6.1 simulated more dust > 5 μm and less dust < 5 μm than CAM6.α. However, both models underestimated the observed mass fraction of dust in that size range at the high-atmosphere level (6-7 km) near the Cabo Verde. The models also fail to capture the change in the size distribution between the two atmospheric levels that the measurements suggest.

4.2 Impacts of each modification on the dust cycle modeling

555   The next sections detail the relative importance of each modification to the modeled dust properties (loading, and/or other dust variables). We show in Sect. 4.2.1-4.2.3 the results on the global mean and spatial distribution, and in Sect. 4.2.4 how the modifications affect the dust properties on the regional mean basis.

4.2.1 Dust emission schemes: BRIFT versus DEAD

The dust emission in MIINE_NEW_EMIS using BRIFT (2910 Tg a^{-1}) is 35% lower than in MINE_BASE using DEAD
560   (4456 Tg a^{-1}), primarily due to the lower DOD (0.035 versus 0.029) and higher dust lifetime in the former (3.1 and 2.2 days) (Table 4). The relative strength of dust emission for different sources also differs between DEAD and BRIFT, as Kok et al. (2011b) documented based on CAM4. The comparison between the two emission schemes here on the spatial distribution of the dust emission largely remains as in CAM4. For example, the preferential source function of Zender et al. (2003b) used in DEAD simulates most of the emission in the central part of North Africa (e.g., the Bodélé depression) (Fig. 2a). In
565   comparison, the dust emission coefficient in BRIFT (see Eq. 7a of Kok et al., 2011b) and the new method of calculating the threshold gravimetric water content of the topsoil layer shifts the main dust emission in North African source westward and

southward into the dust source belt (higher dust emission fluxes relative to the other source regions Fig. 2b versus Fig. S11 and Kok et al., 2011b). This shifting in BRIFT, compared to DEAD, tends to have the dust emission to occur in the wind erodible areas that satellite-based retrievals suggest (Ashpole and Washington, 2013; Ginoux et al., 2012), though the

570 retrieval of dust beneath clouds are unavailable which may lead to a missing of potential dust sources that satellite retrievals cannot detect, for example, dust emissions occur at the presence of deep convection (Engelstaedter and Washington, 2007; Marsham et al., 2013). The much lower dust emission in Taklimakan and Gobi deserts in China relative to that from North Africa using BRIFT, concerning that comparison using DEAD (Fig. 2b), is likely due to the high soil moisture simulated in CAM6.

575

Another pronounced difference in the modeled dust emission occurs in less erodible areas (i.e., North America, South Africa, Australia), where BRIFT tends to decrease the emission flux compared to using DEAD, an opposite response than that simulated for the North African sources. Such as in Australia, both schemes simulate the maximum in dust emission from the Great Artesian Basin and the Murray-Darling Basin, but BRIFT reduces the dust emission there, bringing a better

580 agreement on the climatological DOD with AERONET observations than DEAD. However, BRIFT, using the unity tuning factor to calculate the threshold gravimetric water content, simulates high dust emissions in western Australia instead of central and eastern Australia as previously documented (Ginoux et al., 2012). Sensitivity tests suggest that using inversed clay fraction can likely better capture the spatial emission pattern in Australia (Fig. S11). In Patagonia, as Kok et al., (2014b) found based on CAM4 simulations, using BRIFT in CAM6.1 substantially increases the dust emission compared to DEAD.

585 In addition, BRIFT simulates the dust emission from a source in northern Chile (the Atacama Desert) and the high-latitude area, where no dust emits in DEAD.

In response to the change in dust emissions due to shifting from DEAD to BRIFT, the global annual mean dust deposition and loadings decreased by 35% and 7%, respectively (Table 4). Considering the lower global DOD in BRIFT than in DEAD

590 (0.035 versus 0.029), differences between the global annual mean dust deposition in BRIFT and DEAD would become smaller, if we rescaled the value according to the same DOD criteria. The change in the total dust deposition and loading (burdens as well; see Fig. 2d versus Fig. 2c) has a similar spatial distribution (Fig. 6a versus Fig. 6b): a great increase of dust deposition and loading primarily in the Southern Ocean, the Middle East, the western Atlantic Ocean, and western USA and its downwind areas, and a great decrease in the Pacific Ocean due to reduced dust emissions in East and Central Asia (Fig.

595 2b); near Greenland, BRIFT simulates more dust deposition and slightly less dust loadings, owing to the local dust emission that occurs in BRIFT (Fig. 2b) but not in DEAD (Fig. 2a) and the ability of transporting further in BRIFT because of the increased lifetime of dust (Table 4).
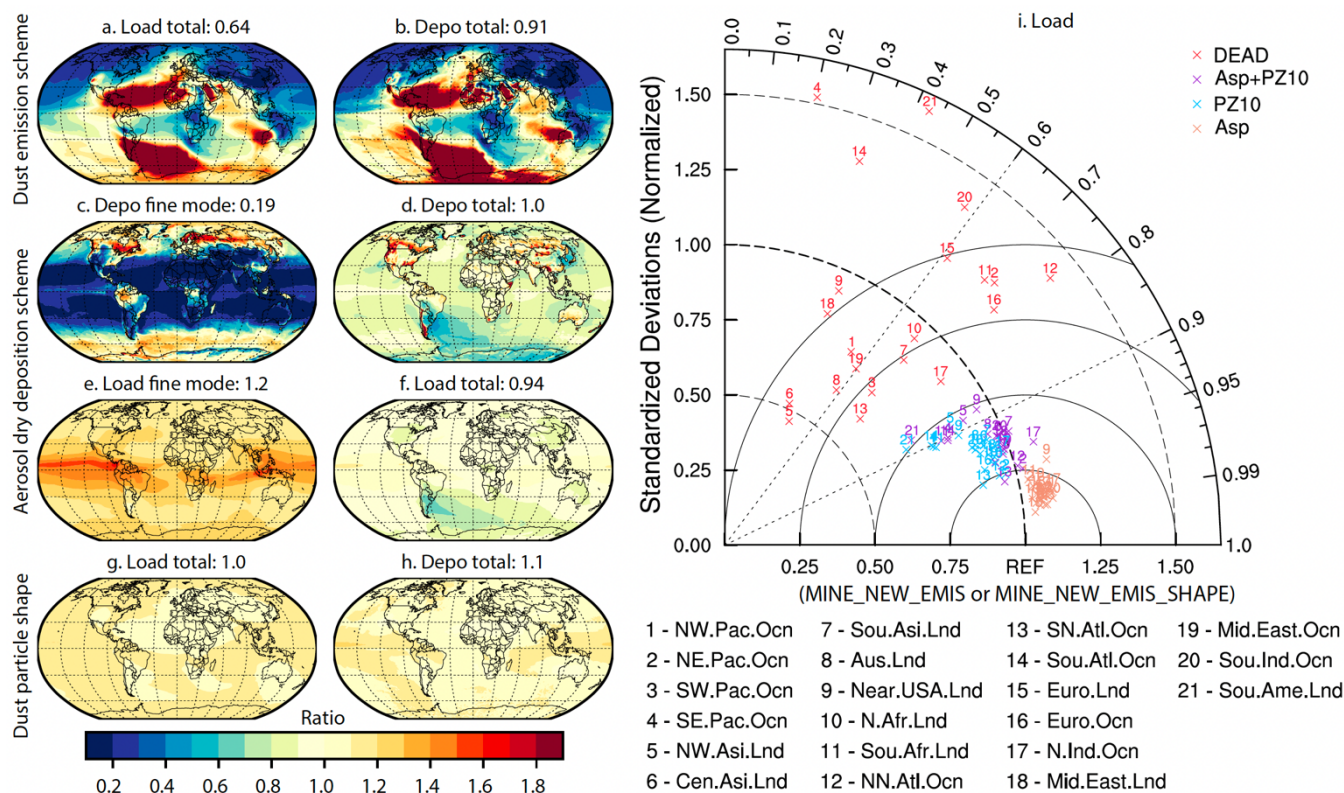
Figure 6. Impacts of the dust emission scheme (a and b: ratio of BRIFT to DEAD), aerosol dry deposition scheme (c-f: ratio of PZ10 to Z01), and dust shape (g and h: ratio of ellipsoidal to spherical dust) on the modeled dust deposition (total: a, d, and g; fine mode: c), and dust loading (total: b, f, and h; fine mode: e). The Taylor diagram (i) compares dust loading in 21 sub-regions defined in Fig. S12. In panels i, DEAD shows comparison between MINE_BASE and MINE_NEW_EMIS; Asp+PZ10 between CAM6.α_MINE and MINE_NEW_EMIS; PZ10 between CAM6.α_MINE and MINE_NEW_EMIS_SHAPE; the Kendall's τ temporal correlation and the standard deviation were obtained based on monthly values with the seasonal cycle removed.

Interestingly, we also find considerable changes to the simulated mass fraction of dust minerals between using BRIFT and DEAD (Fig. S13). These changes are as expected, given the redistributed "hot spots" where dust emission occurs by switching to BRIFT (Fig. 2) and the grid-dependency of the soil mineralogy that we used to initialize the dust speciation (Fig. 1 of Scanza et al., 2015 or Fig. S2 of Li et al., 2011). This change in the simulated mineral mass fractions of dust matters for quantifying the dust shortwave DRE at the top of the atmosphere (hematite) (Balkanski et al., 2007; Li et al., 2021; Sokolik and Toon, 1999), the cloud-aerosol interaction (feldspar) (Atkinson et al., 2013), and biogeochemistry effect (irons) (Mahowald et al., 2011a). It, thus, deserves quantifying how the shift of dust sources changes the simulated mineral content of iron-bearing minerals including hematite, illite and feldspar in the dust. The results suggest that BRIFT simulated ten times more hematite than DEAD in terms of mass (or volume) fraction in the Northern Hemisphere (BRIFT: 1.0%; DEAD: 0.098%) and 25% less in the Southern Hemisphere (BRIFT: 1.2%; DEAD: 1.6%). Such a decreasing of the

simulated mass fraction of hematite aerosol in the Southern Hemisphere is due primarily to reduced dust emission from the Australian deserts, the soil of which enriches iron oxides (Claquin et al., 1999; Journet et al., 2014). BRIFT also shifts the dust emission westward in Australia where the soil abundance of hematite is lower than in the Australian deserts. Similarly,

620   the increased mass fraction of hematite aerosol in the Northern Hemisphere can be partially attributed to the reduced dust emission from East Asia. The change is also evident (increase with the |relative change| > 30%) to feldspar in the South Ocean (Fig. S13d) and to calcite in the North Pacific Ocean (decreasing; Fig. S13f), which may have implications for the amount of the ice nucleation by mineral dust since this nucleation could be dominated by feldspar in mixed-phase clouds (Atkinson et al., 2013).

4.2.2 Dust deposition schemes: PZ10 vs Z01

The comparison of the dry deposition velocity between PZ10 and Z01 is size dependent. Because of the reduced dry deposition velocity in the fine mode, moving to PZ10 from Z01 greatly decreases the dry deposition of fine-mode (accumulation plus Aitken) dust within the low-to-mid latitude regions (between 40º S and 40º N; Fig. 6c; PZ10:Z01<0.3; similar in the accumulation mode only as Fig. S14b suggests). Since most dust mass is in the coarse mode, the small change

630   of dust deposition in this mode, because of the slightly larger dry deposition velocity in the coarse mode in PZ10 than in Z01, results in a slight change in the total dust deposition in the low-to-mid latitude regions (Fig. 6d or Fig. S15b). Even for dust deposition in the fine mode, the increased wet deposition by using PZ10 (such as in the accumulation mode shown in Fig. S16b) offsets the reduced dry deposition in the low-to-mid latitude regions, resulting in a negligible change spatially and on global average (not shown). In the South Ocean (downwind of the Patagonian deserts), a decrease of dry deposition

635   fluxes causes more fine-mode dust aerosol particles near the source regions, which then become cloud-borne, leading to an increase of the dry deposition flux at the downwind regions (Fig. 6c). But the reduced dust deposition in the coarse mode dominates over the increased dry deposition flux at the downwind regions, leading to a considerable decrease of total dust deposition by >30% (relative change; Fig. 6d).

640   Compared to Z01, PZ10 increased the global mean dust loading in the fine mode by ~20% (Fig. 6e). Particularly in the tropics, such an increase in the remote areas can be over 60%, though the dust abundance there is low. The slight decrease of dust in the coarse mode dominates the change in the total dust loading, resulting in a slight decrease of the global mean total dust loading by 6% (Fig. 6f). Correspondingly, the global mean DOD remains almost the same between the simulations using PZ10 and Z01 (Table 4).

4.2.3 Dust asphericity

Matching modelled DOD to observations requires the model to account for the dust asphericity, which acts to enhance the mass extinction efficiency of particles, particularly in the coarse mode (Kok et al., 2017). This enhancement in the mass extinction efficiency due to the dust asphericity is not included in the current version of CESM2 but will be incorporated into

650   a future officially released CESM2 version. According to calculations of Kok et al., (2017), the dust mass extinction efficiency at the visible band due to dust asphericity is approximately 16% and 28% higher for non-spherical particles than for spherical particles in the fine (accumulation plus Aitken) and coarse modes, respectively. Consequently, the model requires lower dust emissions to achieve a global DOD of ~0.030 compared to simulations without considering dust asphericity. The shape effect on the mass extinction efficiency may also explain the difference between the global mean DOD in AEROCOM (Aerosol Comparisons between Observations and Models; median: 0.023; Huneeus et al., 2011) and

655   Ridley et al., (0.03 ± 0.005; 2016) near the visible band. We have included the enhanced dust mass extinction efficiency due to dust asphericity in our previous studies (e.g., Li et al., 2021, Kok et al.,2021) and in all the simulations here. It suggests that inclusion of this enhanced dust mass extinction efficiency would reduce the overestimation of the surface concentration (Kok et al.,2021). Here we do not document more its impact on the simulated dust cycle.

660   The overall change to the spatial distribution of dry deposition induced by dust asphericity is not as important as the change induced by changing to the dry deposition scheme PZ10. The model simulated a similar overall spatial distribution of dust deposition at the surface between modeling dust as spherical and ellipsoid shaped particles (Fig. 6h). The lower gravitational settling velocity when modeling dust as ellipsoids induced a considerable change to dust deposition only locally within remote areas: the South Pacific, western and eastern equatorial Pacific, and downwind of Patagonia, an increase of the dry

665   deposition by up to 30% (MINE_NEW_EMIS_SHAPE versus MINE_NEW_EMIS). In comparison, little change to the dust deposition by dust asphericity occurs near/over major dust source regions. This contrast in the changes in the dry deposition flux between close-to-source and remote areas suggests that including dust asphericity could potentially mediate the overestimated dust emission from source regions (e.g., North Africa).

4.2.4 Dust size representation

670   The removal rates of dust aerosol particles highly depends on their size (Mahowald et al., 2014). Since dust in the coarse mode accounts for most of the dust loading, changing the coarse-mode size distribution (σ, GMD, and the prescribed minimal and maximum boundaries within which GMD can vary, Table 1) from the coarse-mode σ used in CAM6.1 (S5; σ or GSD=1.2; lifetime=4.3 days; Table 4) to that in NEW_EMIS_SIZE (S5; σ or GSD=1.8; lifetime=2.4 days; Table 4) reduced the lifetime of dust by a half and thus also reduced the dust loading (Fig. 7b). This decrease of dust lifetime is primarily due

675   to the change in σ (GSD) of the coarse mode (Fig. 7b) rather than the prescribed GMD and its boundaries, as we obtained almost the same dust lifetime (~2.4 days) between NEW_EMIS_SIZE and NEW_EMIS_SIZE_WIDTH (Table 4). The impact of the other differences (e.g., bulk versus speciated dust and BRIFT versus DEAD; note NEW_EMIS, NEW_EMIS_SIZE, and NEW_EMIS_SIZE_WIDTH are using the same method, different from CAM6.α and the speciated dust runs, to compute the threshold gravimetric water content above which the impression of dust emission due to soil

680   moisture occurs) on the simulated dust lifetime seems trivial (e.g., between different emission schemes, CAM6.1: lifetime=4.3 days versus NEW_EMIS: lifetime=4.9 days). Correspondingly, given a similar emission rate, DOD has a strong

response to the change in the coarse mode σ (GSD) (NEW_EMIS_SIZE_WIDTH: DOD=0.019 versus NEW_EMIS: DOD=0.030; absolute relative change≈37%≈ (0.030-0.019)/0.030*100). Since the GMD predicted in the model varies little, the prescribed GMD boundaries does not affect the DOD calculation. We can, therefore, derive that the prescribed GMD

685   itself, which initiates the online calculations of the GMD, is also relevant to the DOD calculation (NEW_ EMIS_SIZE: DOD=0.013 versus NEW_ EMIS_SIZE_WIDTH: DOD=0.019; absolute relative change=20%=(0.019-0.013)/0.030*100) but second to the influence of the coarse-mode σ(GSD).
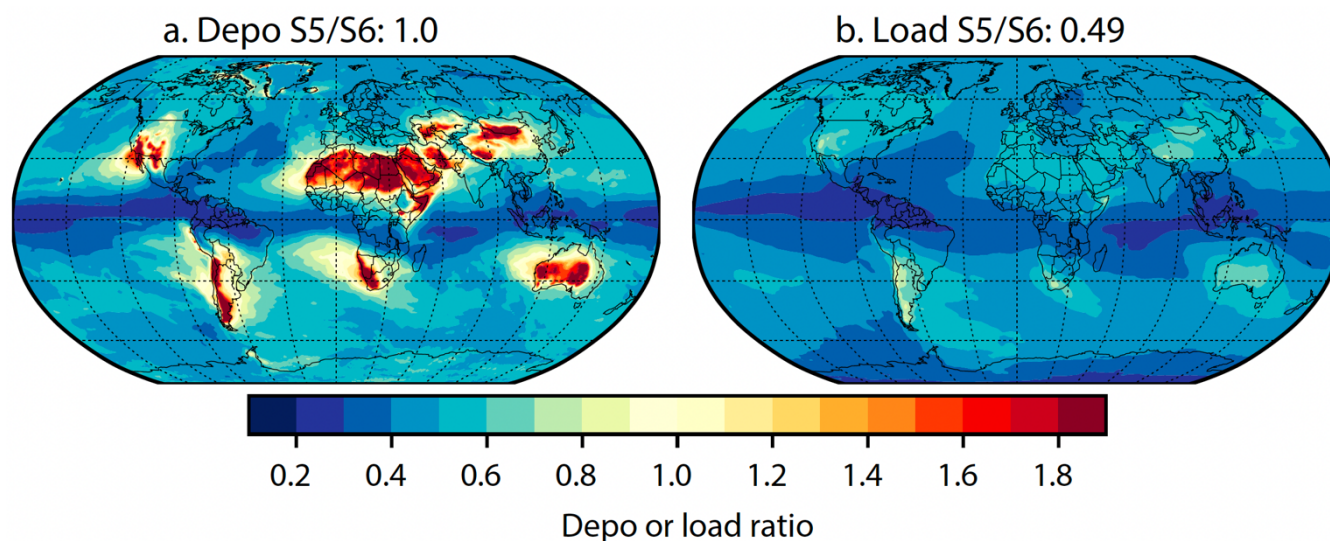
Figure 7. Impact of changing the coarse-mode geometric standard deviation (GSD or σ) for transported dust aerosol on the modeled dust

690   surface deposition fluxes (depo) and column loading (load): ratio of NEW_EMIIS (S5: σ =1.8) to NEW_EMIS_SIZE (S6: σ =1.2) (see Table 2 for case names). Numbers on the top of the plot show ratios on global average.

The lifetime of dust also tends to be higher for aerosol particles experiencing strong convection, which uplifts them high above the surface (Cakmur et al., 2004). This mechanism likely partially explains the increased lifetime from 2.2 days in

695   MINE_BASE to 3.1 days in MINE_NEW_EMIS. Due to the southwestward shifting of dust emission in BRIFT to the "real" dust belt in North Africa (Sect. 4.2.1), dust aerosol particles experienced stronger vertical transport (not shown, Li et al. *in prep*) by near-surface convergence that controls the annual cycle of North African dust (Engelstaedter and Washington, 2007). This may in turn indicate the importance of convergence-related convection (i.e., haboob) (Marsham et al., 2011) and where the dust emission occurs on dust transport, especially the cross-Atlantic/Pacific (Prospero, 1999; Prospero et al., 2020)

700   and -equatorial transport (Kok et al., 2021a; Li et al., 2008), which, currently, the models do not well represent.

4.2.5 Impacts of the modifications on the regional mean basis

The regional analysis over 21 selected sub-regions (Fig. S12 for definition) suggests that, over most of those sub-regions, the simulated dust loading/deposition flux using the model under different modifications (PZ10, and/or dust asphericity) except

to the dust emission scheme closely correlates (temporal correlation coefficient > 0.85 based on monthly values) with that in
705   the reference case MINE_NEW_EMIS (Fig. 6i). In addition to slightly increasing dust loading, introducing dust asphericity
to the model slightly increases the temporal variability of the modeled dust loading, while replacing Z01 with PZ10 slightly
decreased the variability of the simulated dust loading with respect to the reference case generally in nearly all the 21 sub-
regions (Fig. 6i). The combined effect of the two modifications on this temporal variability is more determined by the choice
between PZ10 and Z01 than dust asphericity.

710

Using different dust emission schemes changes the regional dust loading/deposition flux the most among those modifications
in terms of the standard deviation (the BRIFT/DEAD ratio>1.25 or <0.75 in many regions) and temporal correlation (low-to-
moderate temporal correlation between 0.15 and 0.85) (Fig. 6i). Particularly, the strong regional contrast on the dust
loading/deposition exists in the northwest Asia (region 5: the BRIFT/DEAD ratio<0.5 and temporal correlation<0.5), Central
715   Asia (region 6: the BRIFT/DEAD ratio<0.6 and temporal correlation<0.5), southeastern Pacific Ocean (region 4: the
BRIFT/DEAD ratio>1.5 and temporal correlation=~0.2), and southern America (region 21: the BRIFT/DEAD ratio>1.5 and
temporal correlation<0.5).

4.3 Dust direct radiative effect

CAM6.α yields a global mean net dust DRE of ~-0.26 W m^{-2} (shortwave plus longwave; longwave has been augmented by
720   51% to include dust scattering), which is slightly less cooling than in CAM6.1 (~-0.30 W m^{-2}). But the net dust DRE can
strongly differ between the two model versions at regional scales (Fig. S17a). For example, CAM6.α suggests more warming
(difference > 2 W m^{-2} in amplitude) near Australia due to reduced dust loadings (or DOD) (Fig. 6a) and hematite mass
fraction (Fig. S17a), and more cooling (difference > 2 W m^{-2} in amplitude) in downwind regions of North Africa primarily
due to increased dust loadings (Fig. 6a). The opposite change in one region relative to another, however, cancels out at the
725   global scale, resulting in a negligible net DRE change (-0.04 W m^{-2}). The following subsections evaluate the model
performance on reproducing the observed dust DRE efficiency (Sect. 4.3.1) and quantify the impact of each modification on
the estimate of dust DRE and its efficiency (Sect. 4.3.2 and 4.3.3).

4.3.1 Dust direct radiative effect efficiency

All model versions as shown in Fig. 8 have difficulty in reproducing the shortwave dust net DRE efficiency (defined as the
730   ratio of dust DRE to DOD) under clear-sky conditions (Fig. 8a). In the shortwave spectral range, the new model, CAM6.α,
does not show improvement, in general. It works better in reproducing the retrievals only in the Atlantic Ocean (10º-30ºN,
20º-45ºW) in the summer and at a site in the Mediterranean basin (33.5ºN, 12.6ºW) in September. Modeling dust as
component minerals with the dust size distribution in coarse mode of CAM6S5 (NEW_EMIS_SIZE) helps improve the
model performance relative to modeling dust as a bulk in four out of the six domains/sites (Fig. 8a). In the longwave spectral
735   range (Fig. 8b), the dust DRE efficiency in the new model, CAM6-α, agrees better with retrievals than that in CAM6.1,

likely mainly owing to the improved representation of the dust cycle. Modeling dust as mineral components (i.e., in CAM6.α_MINE relative to bulk dust) also tends to reduce the overall model bias in the longwave spectral range, though the DRE efficiency in CAM6.α_MINE is at the lower bound of the observation for the broad area of North Africa. This improvement, however, could be artificial because of the imaginary complex refractive index of hematite volume used here

740 (see Fig. 1b of Li et al., 2021) together with the volume mixing used in the dust speciated model to compute the bulk-dust complex refractive index (Li et al. in prep.). Due to the same reason, in the shortwave spectral range, dust simulated in the component dust model tends to be more absorptive than in the bulk dust model (Fig. 8a and Table 4). It worth noting that, in addition to uncertainty due to the imperfect representation of the spatial distribution of dust aerosols (Fig. 1), the different spectral ranges in the model and the satellite-based sensors and radiation parameterization in the model (Jones et al., 2017)

745 may also contribute to the difference between dust DRE efficiency from the model and observations.

All the modifications do not change the global mean longwave efficiency (Table 4), except that BRIFT yields the global mean net efficiency value that substantially differs in the shortwave spectral range compared to DEAD (MINE_NEW_EMIS: -2.1 W m^{-2} τ^{-1} versus MINE_BASE: -4.0 W m^{-2} τ^{-1}; Table 4).
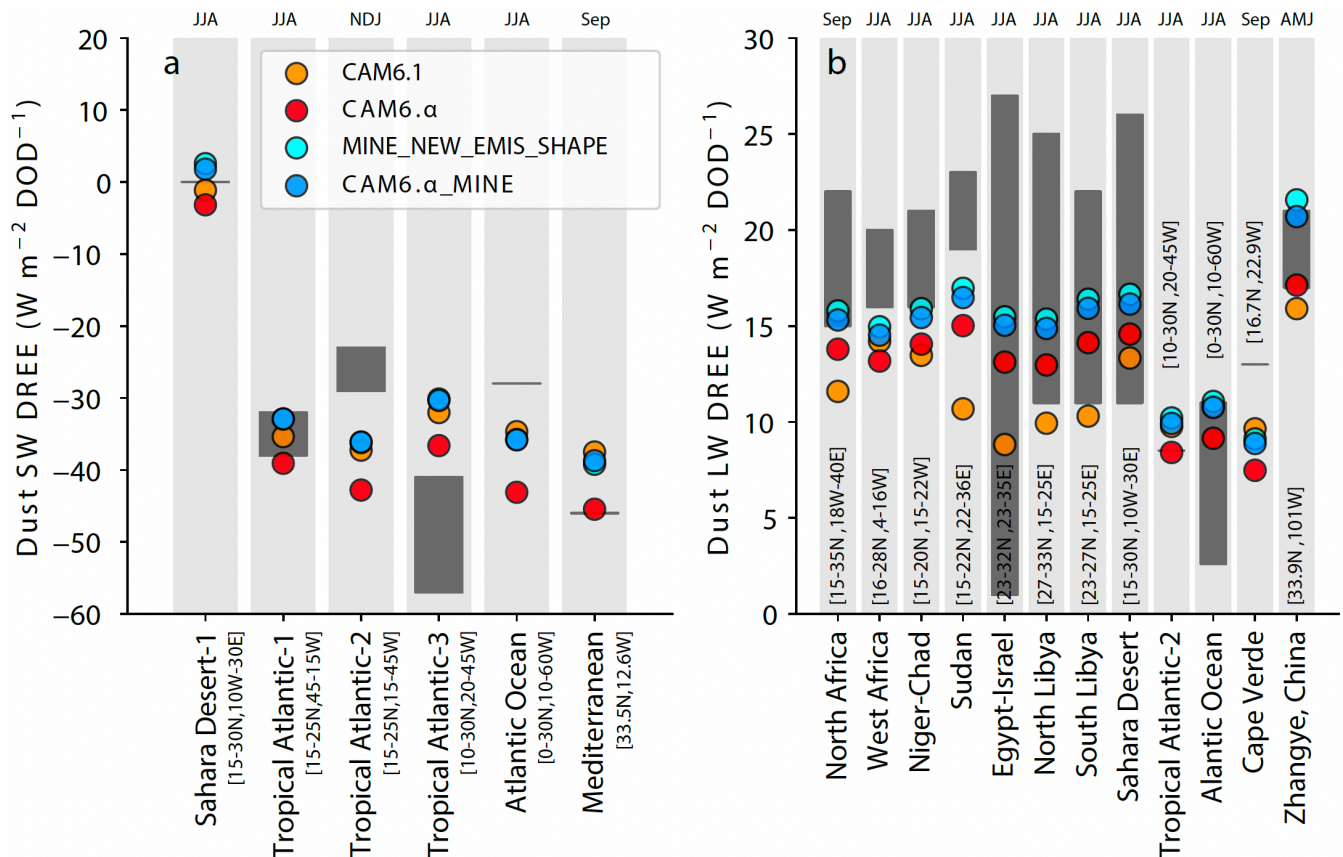
750

Figure 8. Modelled and observed dust direct radiative effect efficiency at the shortwave (SW)/longwave (LW) under clear conditions at the TOA over the sub-domains (shown in the inserted map and location described below) in summer, fall, and September for the 2000s climate. The radiative effect efficiency is defined as the ratio of the radiative effect to DOD, so has units of W m^{-2} τ^{-1}. Included cases from

755 left are CAM6.1, CAM6-α, MINE_NEW_EMIS_SHAPE, CAM6.α _MINE. The field value/range are from references listed in Table 3. Here the LW radiative effect from the model was augmented by 51% to account for the dust scattering (Dufresne et al., 2002).

4.3.2 Impacts of dust asphericity, dry deposition scheme, and dust emission scheme

The dust asphericity introduced negligible (relative change < 10%) impacts on the global net dust DRE, and PZ10 enhanced the net dust cooling by ~18% ($\approx$(0.13-0.11)/0.11*100) relative to that using Z01 (Table 4). Regionally, the slightly

760 higher/lower dust loading or DOD due to dust asphericity only slightly enhanced/weakened the warming over land (Fig. 9a; e.g., North African land; net DRE: 0.97 and 1.1 W m^{-2} for MINE_NEW_EMIS and MINE_NEW_EMIS_SHAPE, respectively; the single scattering albedo at the visible bands ~0.90 for both runs, not shown) / ocean (e.g., downwind of North Africa). PZ10 simulated a slightly enhanced cooling relative to Z01 almost everywhere (Fig. 9b; e.g., south northern Atlantic Ocean, net DRE: 0.72 and 0.76 W m^{-2} for MINE_NEW_EMIS_SHAPE and CAM6.α _MINE, respectively).
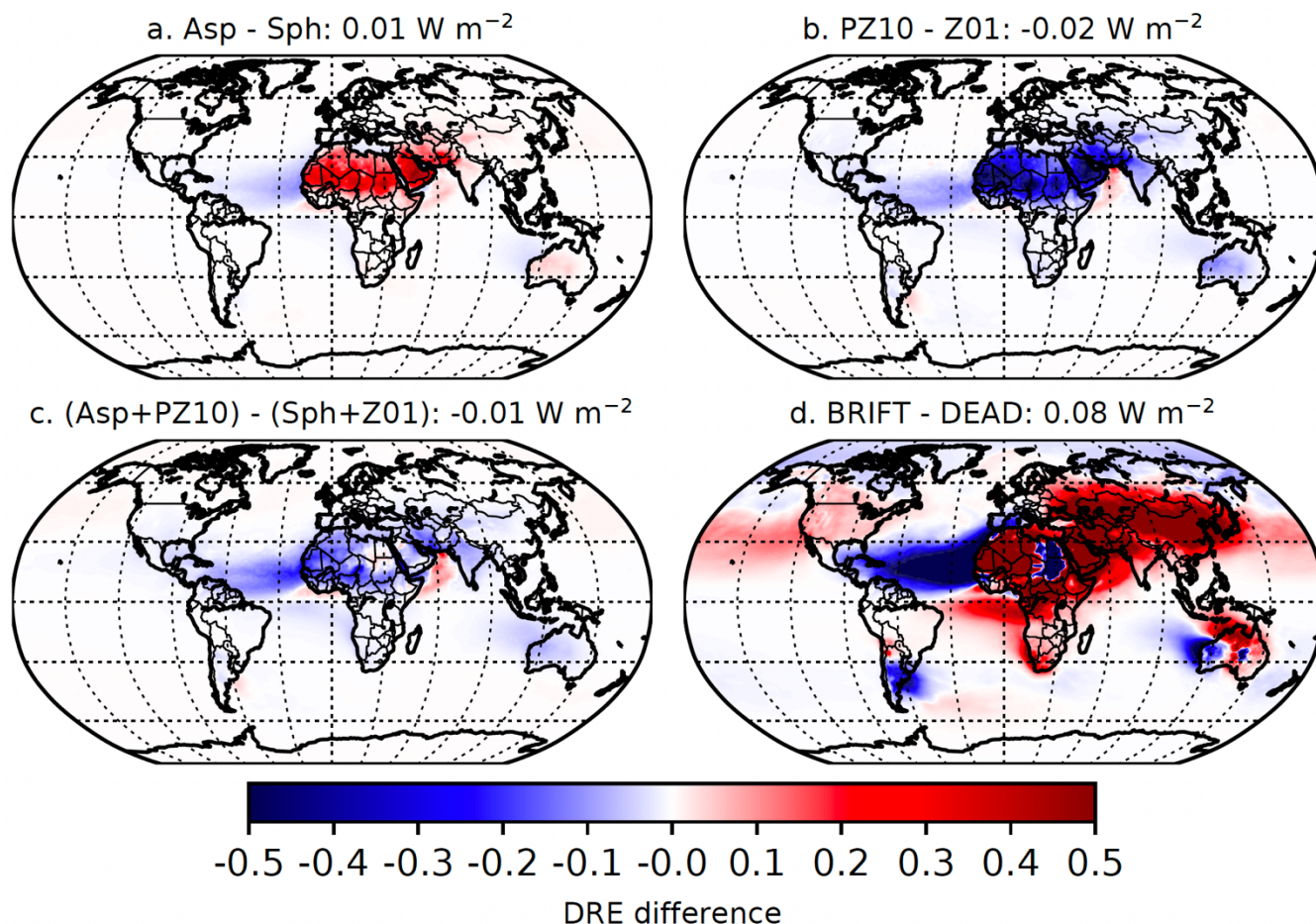
765

Figure 9. Spatial distribution of the net (shortwave plus longwave) direct radiative effect difference at the top of the atmosphere under all-sky conditions in current climate between model results using non-spherical (Asp) and aspherical dust (Sph) (a), PZ10 and Z01 (b), Asp+PZ10 and Sph+Z01 (c), and BRIFT and DEAD (d). The longwave radiative effect was augmented by 51% to account for the dust scattering. Numbers shown in each panel title represents annual mean difference in global average.

Calculations suggest a regionally strongly contrasted change to net dust DRE when shifting from DEAD to BRIFT (Fig. 9d), but the enhanced cooling in one region (i.e., the downwind Atlantic Ocean of North Africa: BRIFT: -0.76 W m^{-2}; DEAD: -0.64 W m^{-2}) and warming in another (i.e., western Africa) cancel out, resulting in a weaker global dust cooling, -0.08 W m^{-2} (Table 4). These regional dust DRE differences primarily result from the regional changes to DOD/dust loadings in response to the spatial change in dust emissions, especially for non-Australian sources. Near Australia, the reduced DOD (Fig. 3) and the hematite mass fraction (Fig. S13a), which is negligible for dust from North Africa, contribute to the reduced cooling in East Asia using BRIFT relative to DEAD.

33

4.3.3 Sensitivity to the size distribution

780   In NEW_EMIS_SIZE, the dust DRE at the shortwave bands at the top of the atmosphere under all-sky conditions is ~-0.39 W m^{-2} (Table 4). In contrast, NEW_EMIS yields approximately 70% and 62% stronger cooling effects of -0.66 W m^{-2} by mineral dust. We attribute this strong shortwave cooling in NEW_EMIS primarily to the greatly overestimated mass fraction of fine dust, which is more scattering than coarse dust. The other parameters, such as the GMD bounds of the coarse mode is also relevant to the shortwave dust DRE calculation, inducing a change of 0.12 W m^{-2} (NEW_EMIS_SIZE minus

785   NEW_EMIS_SIZE_WIDTH), which is only slightly smaller than 0.15 W m^{-2} (NEW_EMIS_SIZE_WIDTH minus NEW_EMIS) resulting from the σ change (from 1.2 to 1.8) (Table 4). Compared to its influence at the shortwave bands, the size change only slightly affected the longwave dust DRE calculation (relative change < 30% ≈ (NEW_EMIS_SIZE - NEW_EMIS) / NEW_EMIS * 100).

790   Spatially, differences (less cooling; absolute difference > 3.5 W m^{-2}) on shortwave dust DRE caused by the size change (from S6 to S5) mainly appear over areas close to the non-reflective dust source regions (e.g., ocean regions adjacent to North Africa and the Middle East, where annual surface albedo at visible band < ~0.2) (Fig. S18a). The coarse mode size change from S6 to S5 systematically reduced the longwave warming over all grid cells (Fig. S18c) primarily due to the σ change, as the other parameters enhanced the warming effect instead (Fig. S18d).

795   **4.4 Relative importance of each modification**

Figure 10 compares the relative importance of each modification on the modeled dust quantities and the dust DRE at grid cell scales and on the global average. Overall, replacing the size distribution of dust aerosol and the dust emission scheme with new ones (PZ10 and BRIFT, respectively) are more influential on the modeled quantities of dust (DOD, burden, and deposition) and its DRE estimate, compared to the other modifications. At model grid cell scales, this is especially true for

800   close-to-source regions: the size change dominates over all the others to be the most important factor in modeling the surface dust concentration which occurs everywhere (Fig. 10a); the choice of dust emission scheme is most important in modeling the dust burden (Fig. 10b) and DOD (Fig. 10c) and in estimating the dust DRE. Dust asphericity can only dominate the change to the modeled dust burden and deposition in the South Pacific Ocean (Fig. 10b, d), where the dust mass is low relative to close-to-source regions. As for the dry deposition scheme, switching to PZ10 dominated the change to DOD in the

805   Indian Ocean and equatorial northeastern Pacific Ocean (Fig. 10c), and to the dust lifetime at the north polar region (Fig. 10e) where the total dust is more in the fine mode for which PZ10 reduced the dry deposition velocity (Petroff and Zhang, 2010).

On global average (Fig. 10g), the size change is most important in modeling most of the dust quantities, except deposition
810   for which the choice of the dust emission schemes becomes more influential, and in estimating the dust DRE at the top of the
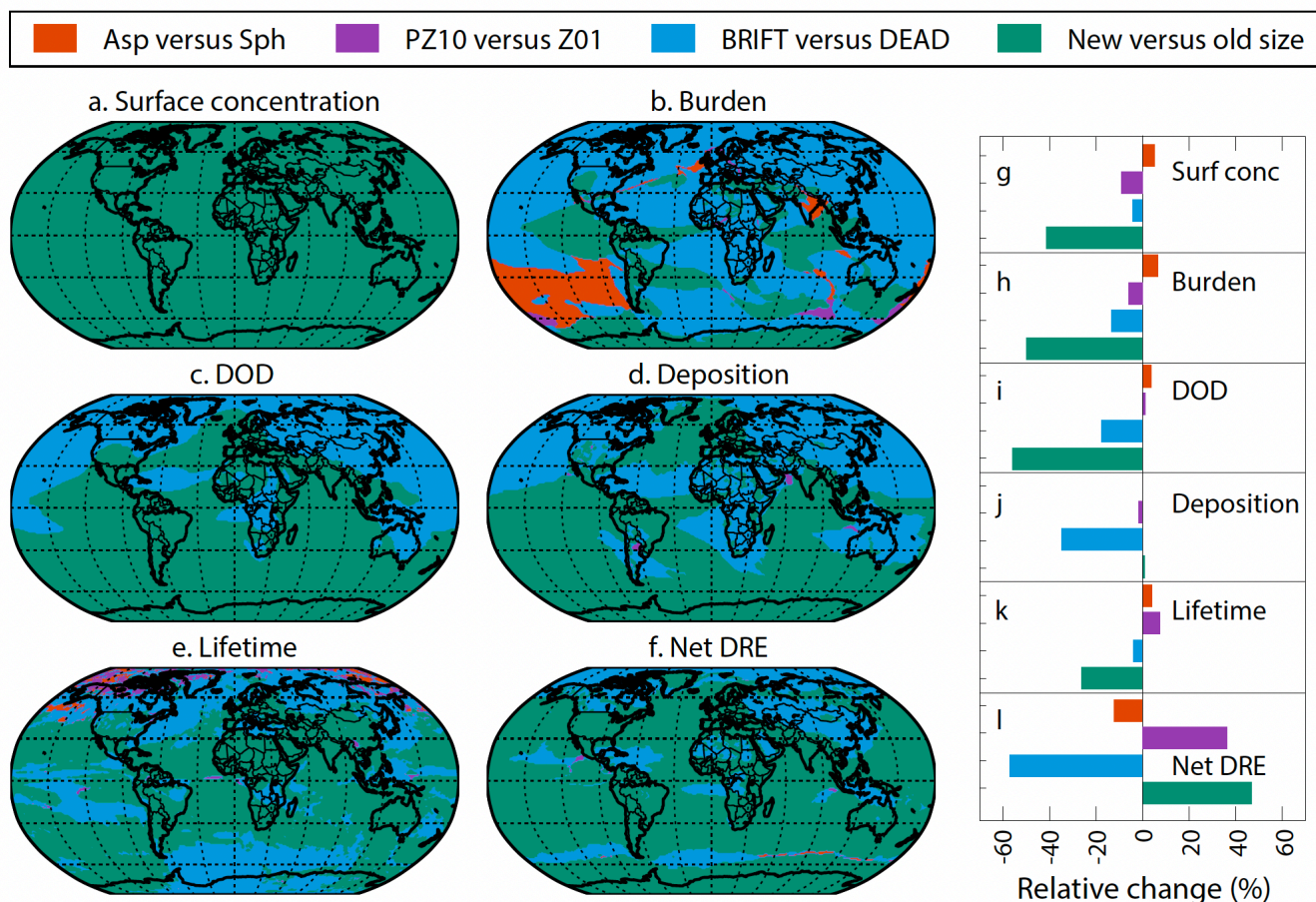atmosphere.

Figure 10. Summary of the relative importance of the modifications (spherical, Sph versus non-spherical dust, Asp; default dry deposition
scheme, Z01 versus new, PZ10; DEAD versus BRIFT dust emission scheme; and coarse-mode size distribution used in CAM5, CAMS5
815   versus that used in CAM6.1, CAMS6) at grid cell levels (panel a-f) and in global average (panel g-i) on surface concentration (a and g),
burden (b and h), DOD (c and i), surface deposition (d and j), lifetime (e and k), and net DRE (f and i) from simulations with offline
dynamics.

5 Limitation in the model-observation comparison

There are issues which may affect the model-observation comparison, when interpreting the comparison: 1) the period when
820   the measurements were made not perfectly matching when the simulations were performed for; 2) different representative
space volume between the model results and observations; the model results are representative of a space volume which is
determined by the spatial resolution and often too large compared to the volume that observations represent (Hamilton et al.,

2019; Wang et al., 2014). Ground stations measure dust-related quantities using stationary instruments, and aircraft-onboard instrument measures dust along with the flight track; 3), some observations include dust of size > 10 µm in diameter

825 (between 10-20 µm; the super coarse dust particles are also present over the source regions and regions downwind of North Africa as found Ryder et al. in 2019, but nearly all the observational constraints used in this study do not include those super coarse dust particles) which our models do not simulate; this might be an important error source (Adebiyi and Kok, 2020). On the other hand, the observations of PM_{10} are likely to include only $PM_{6.9}$, because what measured is in aerodynamic not geometric diameters (Huang et al., 2021; Reid et al., 2003b). Finally, the modelled dust mass is for dust with our own

830 defined mineralogy composition only (Li et al., 2021; Scanza et al., 2015), but the measured mass could likely also include non-dust particles, such as sea salt (Kandler et al., 2011; Zhang et al., 2006), sulfate (Kandler et al., 2007), biomass burning aerosols (Ansmann et al., 2011; Johnson et al., 2008), or other air pollution aerosol (Huang et al., 2010; Yuan et al., 2008), which can get mixed with dust aerosol particles during the transport and may not be completely excluded in the measurements. This contamination of non-dust aerosols on the measurement is especially for dust in the fine-mode size

835 where the instrument cannot distinguish dust from the fine-sized non-dust aerosols; 4) some of observations were not made for a period long enough to be taken as a representative of climatology (see Table 3); also considering point 1), the model-observation comparison may be subject to change because of interannual variability or the episodic character of dust aerosols (Mahowald et al., 2011; also shown in CAM6.1 here); 5) uncertainty in the measurements. In addition to contamination of non-dust aerosols on the measurement of dust, there is also uncertainty due to assumed dust shape and complex refractive

840 index to derive dust size, particularly for particles > 1 µm (Laskin et al., 2006), and error in AERONET AOD retrievals (i.e., the cloud-screening algorithms; Levy et al., 2010) and in the method used to filter out the contribution of non-dust aerosols to the MODIS AOD (see Table 3); note difference exits between clear-sky from observations and all-sky AOD/DOD from the model and aerosol models but the difference is not a considerable error source (tested; not shown); and 6) the method of selecting AERONET sites may introduce uncertainty because of the possible mismatch between simulated and observed

845 AOD for both dust and non-dust aerosols.

6 Concluding remarks and outlook

This study compares how different modelling representations of the dust emission schemes, the aerosol dry deposition schemes, transported dust particle size distributions, and the dust shape treatments affect the modeled dust cycle in CESM2-CAM6.1. We evaluated model performance using different combinations of those modifications using offline dynamics by

850 comparing the modeled dust properties (DOD, dust surface concentrations, dust deposition fluxes, atmospheric size distribution of transported dust, and dust direct radiative efficiency at the top of the atmosphere) that are related to the dust lifecycle with (semi-) observations in the current climate. Since the new more physically based dust emission scheme shows substantial improvements on the model-observation comparison and the updated aerosol dry deposition scheme corrects the overestimated fine-mode deposition velocity, future model developments will be focused on introducing both these features

855 into a future official CAM version for the benefit and use of the whole community. Results of this work therefore inform modelers how well these new features will improve model performance in reproducing the dust cycle in CESM.

Our analysis suggests that the most important change we introduced to CAM6.1 was to revert the geometric standard deviation (σ) of the transported dust size distribution (coarse mode) from 1.8 (as in CAM5) to 1.2, followed by the enhanced
860 dust mass extinction efficiency at the visible band by ~30% to account for the enhancement by dust asphericity (Kok et al., 2017). With the global DOD similarly comparable in different cases because of the retuning we applied or slight impacts by the updates on DOD, the modifications on dry deposition and emission schemes, as well as the gravitational settling due to dust asphericity only slightly changed the simulated seasonal dust loadings/burden/DOD and deposition. However, regionally, large difference among different model results for dust loadings/burden/DOD and deposition are found. These
865 stem either from the choice of the dust emission schemes (BRIFT versus DEAD) or the width of the coarse-mode size distribution. Consequently, it is due primarily to the inclusion of the new dust emission scheme but not use of the new dry deposition scheme and accounting for dust asphericity that the new model, CAM6.α, shows improvements.

Overall, the new model can:
870

1) better capture the climatology and seasonal variation of DOD at more observational sites than the default model, CAM6.1, bearing in mind the uncertainty in the measurement and in the way that we did the model-data comparison;

2) pronouncedly change the regional dust DRE (i.e., stronger warming over most land areas except over South America and
875 stronger cooling over the North Atlantic Ocean; Fig. 9d). Though the opposite change to dust DRE in one region to another partially cancels, (Fig. S17), its influence on the global mean dust DRE remains big (relative change > 55%; Fig. 10l).

Still, there exists large uncertainty in modeling the global and regional dust cycle in comparison with observations. Further development focusing on the following which the current model does not well represent or omits may be helpful for
880 advancing the dust model on simulating the dust cycle in CESM:

1) the threshold friction velocity calculated in both BRIFT and DEAD does not account for the spatiotemporal variability of the soil properties (i.e., soil grain size distribution and aggregate state; Leung et al., 2021; mainly limited by the sparse information; Kok et al., 2014b) in addition to the soil moisture. The current dust module in CAM6.1 also does not consider
885 the roughness effect due to the presence of non-erodible elements (i.e., rocks, pebbles, and vegetation) on the threshold velocity calculation (Marticorena and Bergametti, 1995);

2) crusted surface layer present at the erodible surface can greatly reduce the wind erodibility by increasing the particle cohesion, and, thus, the dust emission rate, compared to the surface that does not consist of consolidated aggregates (Rice

890   and McEwan, 2001);

3) the models used here did not simulate anthropogenic dust emissions due to human activities (i.e., agricultural practice, such as overgrazing, and fugitive dust from roads and constructions), which may constitute a considerable fraction of the total dust emissions (Ginoux et al., 2012). This could likely be a reason for the underestimated dust emission in the northern

895   high-latitude regions, for instance, at the Moscow metropolitan area (~56ºN, ~37ºE), one of the most significant northern high-latitude sources generated on paved roads and roadside soils (Kasimov et al., 2020), which the current model does not include.

4) as noted in the previous section, the current models do not simulate super coarse dust aerosol particles with diameter

900   greater than > 10 μm which are present in the measurements (Ryder et al., 2018, 2019a).

The comparison of modeling the global and regional dust cycle with observations itself is limited by the spatial and temporal coverage, especially for high-latitude dust including dust in the Southern Hemisphere. More intensive measurements on concentration, deposition, atmospheric loading, and optical properties of dust would help better represent dust and project

905   climate changes in the global climate models. Observational constraints on the dust size distribution are also required, considering its importance for the dust cycle modeling.

Data and code availability

Key model results are available at https://github.com/L3atm/LLi2022GMD. Dust deposition, surface concentrations, and AERONET retrievals (dust optical depth) are available from Albani et al. (2014) and are now available via the GitHub link.

910   DustCOMM data are available at https://dustcomm.atmos.ucla.edu. The updated model code is available upon request and will be available at the GitHub link upon acceptance.

Author contributions (will complete this later)

LL and NMM designed the study. LL updated the CAM6.1, performed all the simulations, analyzed the model results with comments from NMM and JFK, and wrote the original manuscript with comments from NMM. XL and MW provided the

915   new aerosol deposition code. All authors commented and edited the manuscript.

Competing interests

The authors declare that they have no conflict of interest.

Acknowledgements

References

Adebiyi, A., Kok, J., Wang, Y., Ito, A., Ridley, D., Nabat, P. and Zhao, C.: Dust Constraints from joint Observational-
930 Modelling-experiMental analysis (DustCOMM): Comparison with measurements and model simulations, Atmos. Chem.
Phys., 829–863, doi:10.5194/acp-2019-484, 2020.

Adebiyi, A. A. and Kok, J. F.: Climate models miss most of the coarse dust in the atmosphere, Sci. Adv., 6(15), 1–10, 2020.

Albani, S., Mahowald, N. M., Perry, A. T., Scanza, R. A., Zender, C. S., Heavens, N. G., Maggi, V., Kok, J. F. and Otto-
Bliesner, B. L.: Improved dust representation in the Community Atmosphere Model, 2014.

935 Ansmann, A., Petzold, A., Kandler, K., Tegen, I., Wendisch, M., Müller, D., Weinzierl, B., Müller, T. and Heintzenberg, J.:
Saharan Mineral Dust Experiments SAMUM-1 and SAMUM-2: What have we learned?, Tellus, Ser. B Chem. Phys.
Meteorol., 63(4), 403–429, doi:10.1111/j.1600-0889.2011.00555.x, 2011.

Arimoto, R., Ray, B. J., Duce, R. A., Hewitt, A. D., Boldi, R. and Hudson, A.: Concentrations, sources and fluxes of trace
elements in the remote marine atmosphere of New Zealand, J. Geophys. Res., 93(D13), 22389–22405, 1990.

940 Ashpole, I. and Washington, R.: A new high-resolution central and western Saharan summertime dust source map from
automated satellite dust plume tracking, J. Geophys. Res. Atmos., 118(13), 6981–6995, doi:10.1002/jgrd.50554, 2013.

Atkinson, J., Murray, B., Woodhouse, M., Whale, T., Baustian, K., Carslaw, K. S., Doobie, S., O'Sullivan, D. and Malkin,
T.: The importance of feldspar for ice nucleation by mineral dust in mixed-phase clouds, Nature, 498, 355--358
doi:10.1038/nature12278, 2013.

945 Balkanski, Y., Schultz, M., Claquin, T. and Guibert, S.: Reevaluation of mineral aerosol radiative forcings suggests a better
agreement with satellite and AERONET data, Atmos. Chem. Phys., 7, 81–95, 2007.

Di Biagio, C., Di Sarra, A. and Meloni, D.: Large atmospheric shortwave radiative forcing by Mediterranean aerosols
derived from simultaneous ground-based and spaceborne observations and dependence on the aerosol type and single

scattering albedo, J. Geophys. Res. Atmos., 115(10), 1–11, doi:10.1029/2009JD012697, 2010.

950 Brindley, H. E. and Russell, J. E.: An assessment of Saharan dust loading and the corresponding cloud-free longwave direct radiative effect from geostationary satellite observations, J. Geophys. Res. Atmos., 114(23), 1–24, doi:10.1029/2008JD011635, 2009.

Bullard, J. E.: The distribution and biogeochemical importance of highlatitude dust in the Arctic and Southern Ocean-Antarctic regions, J. Geophys. Res., 122(5), 3098–3103, doi:10.1002/2016JD026363, 2017.

955 Bullard, J. E., Baddock, M., Bradwell, T., Crusius, J., Darlington, E., Gaiero, D., Gassó, S., Gisladottir, G., Hodgkins, R., McCulloch, R., McKenna-Neuman, C., Mockford, T., Stewart, H. and Thorsteinsson, T.: High-latitude dust in the Earth system, Rev. Geophys., 54(2), 447–485, doi:10.1002/2016RG000518, 2016.

Cakmur, R., Miller, R. and Torres, O.: Incorporating the effect of small-scale circulations upon dust emission in an atmospheric general circulation model, J. Geophys. Reserach, 109(D07201), doi:10.1029/2003JD004067, 2004.

960 Christopher, S. A. and Jones, T.: Satellite-based assessment of cloud-free net radiative effect of dust aerosols over the Atlantic Ocean, Geophys. Res. Lett., 34(2), 4–7, doi:10.1029/2006GL027783, 2007.

Claquin, T., Schulz, M. and Balkanski, Y. J.: Modeling the Minerology of Atmospheric Dust Sources, J. Geophys. Res. Res., 104(D18), 22243–22256, 1999.

Cwiertny, D. M., Young, M. A. and Grassian, V. H.: Chemistry and photochemistry of mineral dust aerosol, Annu. Rev.
965 Phys. Chem., 59, 27–51, doi:10.1146/annurev.physchem.59.032607.093630, 2008.

Dana, M. T. and Hales, J. M.: Statistical Aspects of the Washout of Polydisperse Aerosols, Atmos. Environ., 10, 45–50, 1976.

Delmonte, B., Baroni, C., Andersson, P. S., Narcisi, B., Salvatore, M. C., Petit, J. R., Scarchilli, C., Frezzotti, M., Albani, S. and Maggi, V.: Modern and Holocene aeolian dust variability from Talos Dome (Northern Victoria Land) to the interior of
970 the Antarctic ice sheet, Quat. Sci. Rev., 64, 76–89, doi:10.1016/j.quascirev.2012.11.033, 2013.

DeMott, P. J., Sassen, K., Poellot, M. R., Baumgardner, D., Rogers, D. C., Brooks, S. D., Prenni, A. J. and Kreidenweis, S. M.: African dust aerosols as atmospheric ice nuclei, Geophys. Res. Lett., 30(14), 1732, doi:10/1029/2003GL017410, 2003, 2003.

Dubovik, O., Smirnov, A., Holben, B. N., King, M. D., Kaufman, Y. J., ECK, T. F. and Slutsker, I.: Accuracy assessments of
975 aerosol optical properties retrieved from Aerososl Robotic Network (AERONET) Sun and sky radiance measurments, J. Geophys. Res., 105(D8), 9791–9806, 2000.

Dufresne, J.-L., Gauier, C., Ricchiazzi, P. and Rouquart, Y.: Longwave Scattering Effects of Mineral Aerosols, Am. Meteorlogical Soc., 59, 1959–1966, 2002.

Easter, R. C., Ghan, S. J., Zhang, Y., Saylor, R. D., Chapman, E. G., Laulainen, N. S., Abdul-Razzak, H., Leung, L. R., Bian,
980 X. and Zaveri, R. A.: MIRAGE: Model description and evaluation of aerosols and trace gases, J. Geophys. Res. D Atmos., 109(20), 1–46, doi:10.1029/2004JD004571, 2004.

Emerson, E. W., Hodshire, A. L., Debolt, H. M., Bilsback, K. R. and Pierce, J. R.: Revisiting particle dry deposition and its

role in radiative effect estimates, Proc. Natl. Acad. Sci., 1–7, doi:https://doi.org/10.1073/pnas.2014761117, 2020.

Engelstaedter, S. and Washington, R.: Atmospheric controls on the annual cycle of North African dust, J. Geophys. Res.
985   Atmos., 112(3), 1–14, doi:10.1029/2006JD007195, 2007.

Eyring, V., Bony, S., Meehl, G. A., Senior, C. A., Stevens, B., Stouffer, R. J. and Taylor, K. E.: Overview of the Coupled
Model Intercomparison Project Phase 6 (CMIP6) experimental design and organization, Geosci. Model Dev., 9(5), 1937–
1958, doi:10.5194/gmd-9-1937-2016, 2016.

Fecan, F., Marticorena, B. and Bergametti, G.: Parameterization of the increase of the aeolian erosion threshold wind friction
990   velocity due to soil moisture for arid and semi-arid areas, Ann. Geophys. Hydrospheres Sp. Sci., 17, 149–157, 1999.

Fécan, F., Marticorena, B. and Bergametti, G.: Parametrization of the increase of the aeolian erosion threshold wind friction
velocity due to soil moisture for arid and semi-arid areas, Ann. Geophys., 17(1), 149–157, doi:10.1007/s00585-999-0149-7,
1998.

Ghan, S. J. and Zaveri, R. A.: Parameterization of optical properties for hydrated internally mixed aerosol, J. Geophys. Res.
995   Atmos., 112(10), 1–10, doi:10.1029/2006JD007927, 2007.

Ginoux, P., Prospero, J., Gill, T. E., Hsu, N. C. and Zhao, M.: Global scale attribution of anthropogenic and natural dust
sources and their emission rates based on MODIS deep blue aerosol products, Rev. Geophys., 50,(RG3005,),
DOI:10.1029/2012RG000388, 2012.

Groot Zwaaftink, C. D., Grythe, H., Skov, H. and Stohl, A.: Substantial contribution of northern high-latitude sources to
1000   mineral dust in the Arctic, J. Geophys. Res., 121(22), 13,678-13,697, doi:10.1002/2016JD025482, 2016.

Hamilton, D. S., Scanza, R. A., Feng, Y., Guinness, J., Kok, J. F., Li, L., Liu, X., Rathod, S. D., Wan, J. S., Wu, M. and
Mahowald, N. M.: Improved methodologies for Earth system modelling of atmospheric soluble iron and observation
comparisons using the Mechanism of Intermediate complexity for Modelling Iron (MIMI v.1.0), Geosci. Model Dev., (May),
1–54, doi:10.5194/gmd-2019-84, 2019.

1005   Hamilton, D. S., Moore, J. K., Arneth, A., Bond, T. C., Carslaw, K. S., Hantson, S., Ito, A., Kaplan, J. O., Lindsay, K.,
Nieradzik, L., Rathod, S. D., Scanza, R. A. and Mahowald, N. M.: Impact of Changes to the Atmospheric Soluble Iron
Deposition Flux on Ocean Biogeochemical Cycles in the Anthropocene, Global Biogeochem. Cycles, 34(3), 1–22,
doi:10.1029/2019GB006448, 2020.

Hansell, R. A., Tsay, S. C., Ji, Q., Hsu, N. C., Jeong, M. J., Wang, S. H., Reid, J. S., Liou, K. N. and Ou, S. C.: An
1010   assessment of the surface longwave direct radiative effect of airborne Saharan dust during the NAMMA field campaign, J.
Atmos. Sci., 67(4), 1048–1065, doi:10.1175/2009JAS3257.1, 2010.

Hansell, R. A., Tsay, S. C., Hsu, N. C., Ji, Q., Bell, S. W., Holben, B. N., Welton, E. J., Roush, T. L., Zhang, W., Huang, J.,
Li, Z. and Chen, H.: An assessment of the surface longwave direct radiative effect of airborne dust in Zhangye, China,
during the Asian Monsoon Years field experiment (2008), J. Geophys. Res. Atmos., 117(13), 1–16,
1015   doi:10.1029/2011JD017370, 2012.

Hillamo, R. E., Kerminen, V.-M., Maenhaut, W., Jaffrezo, J.-L., Balachandran, S. and Davidson, C. I.: Size Distributions of

Atmospheric Trace Elements at Dye 3. Greenland - I. Distribution Characteristics and Dry Deposition Velocities, Atmos. Environ., 27A(17/18), 2787–2802, 1993.

Holben, B. N., Eck, T. ., Slutsker, I., Tanré, D., Buis, J. P., Setzer, A., Vermote, E., Reagan, J. A., Kaufman, Y. J., Nakajima, T., Lavenu, F., Jankowiak, I. and Smirnov, A.: AERONET—A Federated Instrument Network and Data Archive for Aerosol Characterization, Remote Sens. Environ., 66, 1–16, doi:https://doi.org/10.1016/S0034-4257(98)00031-5, 1998.

Huang, K., Zhuang, G., Li, J., Wang, Q., Sun, Y., Lin, Y. and Fu, J. S.: Mixing of Asian dust with pollution aerosol and the transformation of aerosol components during the dust storm over China in spring 2007, J. Geophys. Res., 115, 1–13, doi:10.1029/2009jd013145, 2010.

Huang, Y., Kok, J. F., Kandler, K., Lindqvist, H., Nousiainen, T., Sakai, T., Adebiyi, A. and Jokinen, O.: Climate Models and Remote Sensing Retrievals Neglect Substantial Desert Dust Asphericity, Geophys. Res. Lett., 47(6), 1–11, doi:10.1029/2019GL086592, 2020.

Huang, Y., Adebiyi, A. A., Formenti, P. and Kok, J. F.: Linking the Different Diameter Types of Aspherical Desert Dust Indicates That Models Underestimate Coarse Dust Emission, Geophys. Res. Lett., 48(6), 1–12, doi:10.1029/2020GL092054, 2021.

Huneeus, N., Schulz, M., Balkanski, Y., Griesfeller, J., Prospero, J., Kinne, S., Bauer, S., Boucher, O., Chin, M., Dentener, F., Diehl, T., Easter, R., Fillmore, D., Ghan, S., Ginoux, P., Grini, A., Horowitz, L., Koch, D., Krol, M. C., Landing, W., Liu, X., Mahowald, N., Miller, R., Morcrette, J.-J., Myhre, G., Penner, J., Perlwitz, J., Stier, P., Takemura, T. and Zender, C. S.: Global dust model intercomparison in AeroCom phase i, Atmos. Chem. Phys., 11(15), doi:10.5194/acp-11-7781-2011, 2011.

IPCC: Summary for Policymakers. In: Climate Change 2021: The Physical Science Basis. Contribution of Working Group I to the Sixth Assessment Report of the Intergovernmental Panel on Climate Change, Cambridge University Press. [online] Available from: https://www.ipcc.ch/report/ar6/wg1/, 2021.

Jickells, T. D., Dorling, S., Deuser, W. G., Church, T. M., Arimoto, R. and Prospero, J. M.: Air-borne dust fluxes to a deep water sediment trap in the Sargasso Sea, Global Biogeochem. Cycles, 12(2), 311–320, 1998.

John H. Martin, Steve E. Fitzwater, R. M. G.: Iron deficiency limits phytoplankton growth in Antarctic waters, Global Biogeochem. Cycles, 4(Figure 1), 5–12, doi:https://doi.org/10.1029/GB004i001p00005, 1990.

Johnson, B. T., Heese, B., McFarlane, S. A., Chazette, P., Jones, A. and Bellouin, N.: Vertical distribution and radiative effects of mineral dust and biomass burning aerosol over West Africa during DABEX, J. Geophys. Res. Atmos., 113(23), 1–16, doi:10.1029/2008JD009848, 2008.

Jones, A. L., Feldman, D. R., Freidenreich, S., Paynter, D., Ramaswamy, V., Collins, W. D. and Pincus, R.: A New Paradigm for Diagnosing Contributions to Model Aerosol Forcing Error, Geophys. Res. Lett., 44(23), 12,004-12,012, doi:10.1002/2017GL075933, 2017.

Journet, E., Balkanski, Y. and Harrison, S.: A new data set of soil mineralogy for dust-cycle modeling, Atmos. Chem. Phys., 14, 2014–3801, 2014.

Kandler, K., Benker, N., Bundke, U., Cuevas, E., Ebert, M., Knippertz, P., Rodríguez, S., Schütz, L. and Weinbruch, S.:

Chemical composition and complex refractive index of Saharan Mineral Dust at Izaña, Tenerife (Spain) derived by electron microscopy, Atmos. Environ., 41(37), 8058–8074, doi:10.1016/j.atmosenv.2007.06.047, 2007.

Kandler, K., Lieke, K., Benker, N., Emmel, C., Küpper, M., Müller-Ebert, D., Ebert, M., Scheuvens, D., Schladitz, A., Schütz, L. and Weinbruch, S.: Electron microscopy of particles collected at Praia, Cape Verde, during the Saharan Mineral Dust Experiment: Particle chemistry, shape, mixing state and complex refractive index, Tellus, Ser. B Chem. Phys. Meteorol., 63(4), 475–496, doi:10.1111/j.1600-0889.2011.00550.x, 2011.

Kasimov, N. S., Vlasov, D. V. and Kosheleva, N. E.: Enrichment of road dust particles and adjacent environments with metals and metalloids in eastern Moscow, Urban Clim., 32(October 2019), 100638, doi:10.1016/j.uclim.2020.100638, 2020.

Kok, J.: Does the size distribution of mineral dust aerosols depend on the wind speed at emission?, Atmos. Chem. Phys., 11, 10149–10156, 2011a.

Kok, J., Parteli, E., Michaels, T. and Karam, D.: The physics of wind blown sand and dust, Reports Prog. Phys., 75, 106901, 2012.

Kok, J. F.: A scaling theory for the size distribution of emitted dust aerosols suggests climate models underestimate the size of the global dust cycle, Proc. Natl. Acad. Sci. USA, 108, 1016–1021, doi:https://doi.org/10.1073/pnas.1014798108, 2011b.

Kok, J. F., Mahowald, N. M., Fratini, G., Gillies, J. A., Ishizuka, M., Leys, J. F., Mikami, M., Park, M. S., Park, S. U., Van Pelt, R. S. and Zobeck, T. M.: An improved dust emission model - Part 1: Model description and comparison against measurements, Atmos. Chem. Phys., 14(23), 13023–13041, doi:10.5194/acp-14-13023-2014, 2014a.

Kok, J. F., Albani, S., Mahowald, N. M. and Ward, D. S.: An improved dust emission model - Part 2: Evaluation in the Community Earth System Model, with implications for the use of dust source functions, Atmos. Chem. Phys., 14(23), doi:10.5194/acp-14-13043-2014, 2014b.

Kok, J. F., Ridley, D. A., Zhou, Q., Miller, R. L., Zhao, C., Heald, C. L., Ward, D. S., Albani, S. and Haustein, K.: Smaller desert dust cooling effect estimated from analysis of dust size and abundance, Nat. Geosci., 10(4), 274–278, doi:10.1038/ngeo2912, 2017.

Kok, J. F., Adebiyi, A. A., Albani, S., Balkanski, Y., Checa-Garcia, R., Chin, M., Colarco, P. R., Hamilton, D. S., Huang, Y., Ito, A., Klose, M., Li, L., Mahowald, N. M., Miller, R. L., Obiso, V., Pérez García-Pando, C., Rocha-Lima, A. and Wan, J. S.: Contribution of the world's main dust source regions to the global cycle of desert dust, Atmos. Chem. Phys., 21(10), 8169–8193, doi:10.5194/acp-21-8169-2021, 2021a.

Kok, J. F., Adebiyi, A. A., Albani, S., Balkanski, Y., Checa-Garcia, R., Chin, M., Colarco, P. R., Hamilton, D. S., Huang, Y., Ito, A., Klose, M., Leung, D. M., Li, L., Mahowald, N. M., Miller, R. L., Obiso, V., Pérez García-Pando, C., Rocha-Lima, A., Wan, J. S. and Whicker, C. A.: Improved representation of the global dust cycle using observational constraints on dust properties and abundance, Atmos. Chem. Phys., 21(10), 8127–8167, doi:10.5194/acp-21-8127-2021, 2021b.

Laskin, A., Cowin, J. P. and Iedema, M. J.: Analysis of individual environmental particles using modern methods of electron microscopy and X-ray microanalysis, J. Electron Spectros. Relat. Phenomena, 150(2–3), 260–274, doi:10.1016/j.elspec.2005.06.008, 2006.

1085   Leung, D. M., Kok, J. F., Li, L., Natalie, M., Menut, L., Prigent, C., Klose, M. R., García-pando, C. P. and Lawrence, D. M.:
Improving the parameterization of dust emission threshold in the Community Earth System Model (CESM)., 2021.

Levy, R. C., Remer, L. A., Kleidman, R. G., Mattoo, S., Ichoku, C., Kahn, R. and Eck, T. F.: Global evaluation of the
Collection 5 MODIS dark-target aerosol products over land, Atmos. Chem. Phys., 10(21), 10399–10420, doi:10.5194/acp-
10-10399-2010, 2010.

1090   Li, F., Vogelmann, A. M. and Ramanathan, V.: Saharan dust aerosol radiative forcing measured from space, J. Clim., 17(13),
2558–2571, doi:10.1175/1520-0442(2004)017<2558:SDARFM>2.0.CO;2, 2004.

Li, F., Ginoux, P. and Ramaswamy, V.: Distribution, transport, and deposition of mineral dust in the Southern Ocean and
Antarctica: Contribution of major sources, J. Geophys. Res., 113(D10207), doi:10.1029/2007JD009190, 2008.

Li, L., Mahowald, N., Miller, R., Pérez García-Pando, C., Klose, M., Hamilton, D., Gonçalves Ageitos, M., Ginoux, P.,
1095   Balkanski, Y., Green, R., Kalashnikova, O., Kok, J., Obiso, V., Paynter, D. and Thompson, D.: Quantifying the range of the
dust direct radiative effect due to source mineralogy uncertainty, Atmos. Chem. Phys., 21, 3973–4005,
doi:https://doi.org/10.5194/acp-21-3973-2021, 2021.

Liao, H. and Seinfeld, J. H.: Radiative forcing by mineral dust aerosols: sensitivity to key variables, J. Geophys. Res.,
103(D24), 31,631-637,645, 1998.

1100   Liu, X., Ma, P. L., Wang, H., Tilmes, S., Singh, B., Easter, R. C., Ghan, S. J. and Rasch, P. J.: Description and evaluation of
a new four-mode version of the Modal Aerosol Module (MAM4) within version 5.3 of the Community Atmosphere Model,
Geosci. Model Dev., 9(2), 505–522, doi:10.5194/gmd-9-505-2016, 2016.

Mahowald, N.: Aerosol indirect effect on biogeochemical cycles and climate, Science (80-.)., 334(6057),
doi:10.1126/science.1207374, 2011.

1105   Mahowald, N., Ward, D. S., Kloster, S., Flanner, M. G., Heald, C. L., Heavens, N. G., Hess, P. G., Lamarque, J.-F. and
Chuang, P. Y.: Aerosol impacts on climate and biogeochemistry., 2011a.

Mahowald, N., Albani, S., Engelstaedter, S., Winckler, G. and Goman, M.: Model insight into glacial-interglacial paleodust
records, Quat. Sci. Rev., 30(7–8), doi:10.1016/j.quascirev.2010.09.007, 2011b.

Mahowald, N., Albani, S., Kok, J. F., Engelstaeder, S., Scanza, R., Ward, D. S. and Flanner, M. G.: The size distribution of
1110   desert dust aerosols and its impact on the Earth system, Aeolian Res., 15, doi:10.1016/j.aeolia.2013.09.002, 2014.

Mahowald, N. M., D. Muhs, Levis, S., Rasch, P. J., Yoshioka, M., Zender, C. S., Muhs, D. R., Levis, S., Rasch, P. J.,
Yoshioka, M., Zender, C. S. and Luo, C.: Change in atmospheric mineral aerosols in response to climate: last glacial period,
pre-industrial, modern and doubled-carbon dioxide climates , J. Geophys. Res., 111(10), D10202,
doi:10.1029/2005JD006653, doi:10.1029/2005JD006653, 2006a.

1115   Mahowald, N. M., Yoshioka, M., Collins, W. D., Conley, A. J., Fillmore, D. W. and Coleman, D. B.: Climate response and
radiative forcing from mineral aerosols during the last glacial maximum, pre-industrial, current and doubled-carbon dioxide
climates, Geophys. Res. Lett., 33(20), doi:10.1029/2006GL026126, 2006b.

Mahowald, N. M., Engelstaedter, S., Luo, C., Sealy, A., Artaxo, P., Benitez-Nelson, C., Bonnet, S., Chen, Y., Chuang, P. Y.,

Cohen, D. D., Dulac, F., Herut, B., Johansen, A. M., Kubilay, N., Losno, R., Maenhaut, W., Paytan, A., Prospero, J. M.,
1120 Shank, L. M. and Siefert, R. L.: Atmospheric iron deposition: Global distribution, variability, and human perturbations, Ann.
Rev. Mar. Sci., 1, doi:10.1146/annurev.marine.010908.163727, 2009.

Mahowald, N. M., Scanza, R., Brahney, J., Goodale, C. L., Hess, P. G., Moore, J. K. and Neff, J.: Aerosol Deposition
Impacts on Land and Ocean Carbon Cycles, Curr. Clim. Chang. Reports, 3(1), 16–31, doi:10.1007/s40641-017-0056-z,
2017.

1125 Mahowald, N. M. M., Kloster, S., Engelstaedter, S., Moore, J. K. K., Mukhopadhyay, S., McConnell, J. R. R., Albani, S.,
Doney, S. C. C., Bhattacharya, A., Curran, M. A. J. A. J., Flanner, M. G. G., Hoffman, F. M. M., Lawrence, D. M. M.,
Lindsay, K., Mayewski, P. A. A., Neff, J., Rothenberg, D., Thomas, E., Thornton, P. E. E. and Zender, C. S. S.: Observed
20th century desert dust variability: impact on climate and biogeochemistry, Atmos. Chem. Phys., 10(22), 10875–10893,
doi:10.5194/acp-10-10875-2010, 2010.

1130 Marsham, J., Knippertz, P., Dixon, N., Parker, D. and Lister, G.: The importance of representation of deep convection for
modeled dust-generated winds over West Africa during the summer, Geophys. Res. Lett., 38(L16803),
doi:10.1029/2001GL048368, 2011.

Marsham, J. H., Hobby, M., Allen, C. J. T., Banks, J. R., Bart, M., Brooks, B. J., Cavazos-Guerra, C., Engelstaedter, S.,
Gascoyne, M., Lima, A. R., Martins, J. V., McQuaid, J. B., O'Leary, A., Ouchene, B., Ouladichir, A., Parker, D. J., Saci, A.,
1135 Salah-Ferroudj, M., Todd, M. C. and Washington, R.: Meteorology and dust in the central Sahara: Observations from Fennec
supersite-1 during the June 2011 Intensive Observation Period, J. Geophys. Res. Atmos., 118(10), 4069–4089,
doi:10.1002/jgrd.50211, 2013.

Marticorena, B. and Bergametti, G.: Modeling the atmospheric dust cycle: 1. Design of a soil-derived dust emission scheme,
J. Geophys. Res., 100(D8), 16,415-16,430, doi:https://doi.org/10.1029/95JD00690, 1995.

1140 McConnell, C. L., Highwood, E. J., Coe, H., Formenti, P., Anderson, B., Osborne, S., Nava, S., Desboeufs, K., Chen, G. and
Harrison, M. A. J.: Seasonal variations of the physical and optical characteristics of saharan dust: Results from the dust
outflow and deposition to the ocean (DODO) experiment, J. Geophys. Res., 113, 1–19, doi:10.1029/2007JD009606, 2008.

Mccutcheon, A. J., Lutz, S., Williamson, C., Joseph, M., Tedstone, A. J., Vanderstraeten, A., Wilson, S. A., Bonneville, S.,
Anesio, A. M., Yallop, M. L. and James, B.: Mineral phosphorus drives glacier algal blooms on the Greenland Ice Sheet,
1145 Nat. Commun., (2021), 1–11, doi:10.1038/s41467-020-20627-w, 2021.

Meinander, O., Dagsson-waldhauserova, P., Amosov, P., Aseyeva, E., Atkins, C., Baklanov, A., Baldo, C., Barr, S.,
Barzycka, B., Benning, L. G., Enchilik, P., Frolov, D., Gassó, S., Kandler, K., Kasimov, N., Lasne, J., Lewandowski, M.,
Luks, B., Mcquaid, J. B., Moroni, B., Murray, B. J., Möhler, O., Nawrot, A., Nickovic, S., Neill, N. T. O., Pejanovic, G.,
Popovicheva, O. B., Ranjbar, K., Romanias, M. N., Samonova, O., Sanchez-marroquin, A., Schepanski, K., Semenkov, I.
1150 and Sharapova, A.: Newly identified climatically and environmentally significant high latitude dust sources, Atmos. Chem.
Phys. Discuss., (December), 1–74, 2021.

Miller, R. L. and Tegen, I.: Radiative Forcing of a Tropical Direct Circulation by Soil Dust Aerosols, J. Atmos. Sci., 56(14),

2403–2433, doi:10.1175/1520-0469(1999)056<2403:RFOATD>2.0.CO;2, 1999.

Mills, M. J., Schmidt, A., Easter, R., Solomon, S., Kinnison, D. E., Ghan, S. J., Neely, R. R., Marsh, D. R., Conley, A.,
Bardeen, C. G. and Gettelman, A.: Global volcanic aerosol properties derived from emissions, 1990–2014, using
CESM1(WACCM), J. Geophys. Res., 121(5), 2332–2348, doi:10.1002/2015JD024290, 2016.

Neale, R. B., Chen, C., Lauritzen, P. H., Williamson, D. L., Conley, A. J., Smith, A. K., Mills, M. and Morrison, H.:
Description of the NCAR Community Atmosphere Model (CAM 5 . 0), Boulder, CO., 2010.

Patadia, F., Yang, E.-S. and Christopher, S.: Does dust change the clear sky top of atmosphere shortwave flux over high
surface reflectance regions?, Geophys. Res. Lett., 36(L15825), doi:10.1029/2009GL039092, 2009.

Pérez, C., Nickovic, S., Pejanovic, G., Baldasano, J. M. and Özsoy, E.: Interactive dust-radiation modeling: A step to
improve weather forecasts, J. Geophys. Res. Atmos., 111(16), doi:10.1029/2005JD006717, 2006.

Petroff, A. and Zhang, L.: Development and validation of a size-resolved particle dry deposition scheme for application in
aerosol transport models, Geosci. Model Dev., 3, 753–769, doi:10.5194/gmd-3-753-2010, 2010.

Petroff, A., Mailliat, A., Amielh, M. and Anselmet, F.: Aerosol dry deposition on vegetative canopies. Part I: Review of
present knowledge, Atmos. Environ., 42(16), 3625–3653, doi:10.1016/j.atmosenv.2007.09.043, 2008.

Petters, M. D. and Kreidenwei, S. M.: A single parameter representation of hydroscopic growth and cloud condensation
nucleus activity, Atmos. Chem. Phys., 10, 1961–1971, 2007.

Prospero, J. M.: Long-range transport of mineral dust in the global atmosphere: Impact of African dust on the environment
of the southeastern United States, Proc. Natl. Acad. Sci., 96, 3396–3403, 1999.

Prospero, J. M. and Nees, R. T.: Impact of the North African drought and El Niño on mineral dust in the Barbados trade
winds, Nature, 320(April 24, 1986), 735–738, doi:https://doi.org/10.1038/320735a0, 1986.

Prospero, J. M. and Savoie, D. L.: Effect of continental sources on nitrate concentrations over the Pacific Ocean, Nature,
339(June 29, 1989), 687–689, doi:https://doi.org/10.1038/339687a0, 1989.

Prospero, J. M., Barkley, A. E., Gaston, C. J., Gatineau, A., Campos y Sansano, A. and Panechou, K.: Characterizing and
Quantifying African Dust Transport and Deposition to South America: Implications for the Phosphorus Budget in the
Amazon Basin, Global Biogeochem. Cycles, 34(9), doi:10.1029/2020GB006536, 2020.

Pruppacher, H. and Klett, J.: Microphysics of cluods and precipitation, Kluwer Academic Publishers, Boston., 1997.

Pu, B., Ginoux, P., Guo, H., Christina Hsu, N., Kimball, J., Marticorena, B., Malyshev, S., Naik, V., O'Neill, N. T., Pérez
García-Pando, C., Paireau, J., Prospero, J. M., Shevliakova, E. and Zhao, M.: Retrieving the global distribution of the
threshold of wind erosion from satellite data and implementing it into the Geophysical Fluid Dynamics Laboratory land-
atmosphere model (GFDL AM4.0/LM4.0), Atmos. Chem. Phys., 20(1), 55–81, doi:10.5194/acp-20-55-2020, 2020.

R.Arimoto, Duce, R. A., Ray, R. J., Unni, C. K., Arimoto, R., Duce, R. A., Ray, B. and Umni, C.: Atmospheric trace
elements at Enewetak Atoll, 2. Transport to the ocean by wet and dry deposition, J. Geophys. Res., 90, 2391–2408, 1985.

Reid, E., Reid, J., Meier, M., Dunlap, M., Cliff, S., Broumas, A., Perry, K. and Maring, H.: Characterization of African dust
transported to Puerto Rico by individual particle and size segregated bulk analysis, JGR-Atmospheres, 108(D19, 8591),

46

Geoscientific
Model Development
Discussions

doi:10.1029/200dJD002935, 2003a.

Reid, J. S., Jonsson, H. H., Maring, H. B., Smirnov, A., Savoie, D. L., Cliff, S. S., Reid, E. A., Livingston, J. M., Meier, M. M., Dubovik, O. and Tsay, S. C.: Comparison of size and morphological measurements of coarse mode dust particles from

190 Africa, J. Geophys. Res. D Atmos., 108(19), doi:10.1029/2002jd002485, 2003b.

Rice, M. A. and McEwan, I. K.: Crust strength: A wind tunnel study of the effect of impact by saltating particles on cohesive soil surfaces, Earth Surf. Process. Landforms, 26(7), 721–733, doi:https://doi.org/10.1002/esp.217, 2001.

Ridley, D., Heald, C., Kok, J. and Zhao, C.: An observationally-constrained estimate of global dust aerosol optical depth, Atmos. Chem. Phys., doi: 10.5194/acp--2016--385, 2016.

195 Rosenfeld, D., Rudich, Y. and Lahav, R.: Desert dust suppressing precipitation: a possible desertification feedback loop, Proc. Natl. Acad. Sci. U. S. A., 98(11), 5975–5980, 2001.

Ryder, C. L., Highwood, E. J., Rosenberg, P. D., Trembath, J., Brooke, J. K., Bart, M., Dean, A., Crosier, J., Dorsey, J., Brindley, H., Banks, J., Marsham, J. H., McQuaid, J. B., Sodemann, H. and Washington, R.: Optical properties of Saharan dust aerosol and contribution from the coarse mode as measured during the Fennec 2011 aircraft campaign, Atmos. Chem.

200 Phys., 13(1), 303–325, doi:10.5194/acp-13-303-2013, 2013.

Ryder, C. L., Marenco, F., Brooke, J. K., Estelles, V., Cotton, R., Formenti, P., McQuaid, J. B., Price, H. C., Liu, D., Ausset, P., Rosenberg, P. D., Taylor, J. W., Choularton, T., Bower, K., Coe, H., Gallagher, M., Crosier, J., Lloyd, G., Highwood, E. J. and Murray, B. J.: Coarse-mode mineral dust size distributions, composition and optical properties from AER-D aircraft measurements over the tropical eastern Atlantic, Atmos. Chem. Phys., 18(23), 17225–17257, doi:10.5194/acp-18-17225-

205 2018, 2018.

Ryder, C. L., Highwood, E. J., Walser, A., Seibert, P., Philipp, A. and Weinzierl, B.: Coarse and giant particles are ubiquitous in Saharan dust export regions and are radiatively significant over the Sahara, Atmos. Chem. Phys., 15353–15376, doi:https://doi.org/10.5194/acp-19-15353-2019, 2019a.

Ryder, C. L., Highwood, E. J., Walser, A., Seibert, P., Philipp, A. and Weinzierl, B.: Coarse and Giant Particles are

210 Ubiquitous in Saharan Dust Export Regions and are Radiatively Significant over the Sahara, Atmos. Chem. Phys. Discuss., 19, 15353–15376, doi:https://doi.org/10.5194/acp-19-15353-2019, 2019b.

Sarangi, C., Qian, Y., Rittger, K., Ruby Leung, L., Chand, D., Bormann, K. J. and Painter, T. H.: Dust dominates high-altitude snow darkening and melt over high-mountain Asia, Nat. Clim. Chang., 10(11), 1045–1051, doi:10.1038/s41558-020-00909-3, 2020.

215 Scanza, R. A., Mahowald, N., Ghan, S., Zender, C. S., Kok, J. F., Liu, X., Zhang, Y. and Albani, S.: Modeling dust as component minerals in the Community Atmosphere Model: Development of framework and impact on radiative forcing, Atmos. Chem. Phys., 15(1), doi:10.5194/acp-15-537-2015, 2015.

Scanza, R. A., Hamilton, D. S., Perez Garcia-Pando, C., Buck, C., Baker, A. and Mahowald, N. M.: Atmospheric Processing of Iron in Mineral and Combustion Aerosols: Development of an Intermediate-Complexity Mechanism Suitable for Earth

220 System Models, Atmos. Chem. Phys., 18, 14175–14196, doi:10.5194/acp-18-14175-80, 2018.

Shao, Y.: Physics and Modelling of Wind Erosion, 2nd ed., Heidelberg: Springer., 2008.

Shi, Y. and Liu, X.: Dust Radiative Effects on Climate by Glaciating Mixed-Phase Clouds, Geophys. Res. Lett., 46(11), 6128–6137, doi:10.1029/2019GL082504, 2019.

Shi, Y., Liu, X., Wu, M., Ke, Z. and Brown, H.: Relative Importance of High-Latitude Local and Long-Range Transported
1225 Dust to Arctic Ice Nucleating Particles and Impacts on Arctic Mixed-Phase Clouds, Atmos. Chem. Phys. Discuss., (August), 1–57, doi:10.5194/acp-2021-621, 2021.

Shinn, A., Smith, W. and Barber, T.: African Dust and the Demise of Caribbean Coral Reefs, Geophys. Res. Leters, 27(19), 3029–3032, doi:https://doi.org/10.1029/2000GL011599, 2000.

Skiles, S. M. K., Flanner, M., Cook, J. M., Dumont, M. and Painter, T. H.: Radiative forcing by light-absorbing particles in
1230 snow, Nat. Clim. Chang., 8(11), 964–971, doi:10.1038/s41558-018-0296-5, 2018.

Sokolik, I. N. and Toon, O. B.: Direct radiative forcing by anthropogenic airborne mineral aerosols, Nature, 381(June 20, 1996), 681–683, 1996.

Sokolik, I. N. and Toon, O. B.: Incorporation of mineralogical composition into models of the radiative properties of mineral aerosol form UV to IR wavelengths, J. Geophys. Res., 104(D8), 9423–9444, 1999.

1235 Sokolik, I. N., Winker, D. M., Bergametti, G., Gillette, D. A., Carmichael, Y. J., Kaufman, Y. J., Gomes, L., Schuetz, L. and Penner, J. E.: Introduction to special section: Outstanding problems in quantifying the radiative impacts of mineral dust, J. Geophys. Res. Atmos., 106(16), 18015–18027, doi:10.1029/2000jd900498, 2001.

Song, Q., Zhang, Z., Yu, H., Kato, S., Yang, P., Colarco, P., Remer, L. A. and Ryder, C. L.: Net radiative effects of dust in the tropical North Atlantic based on integrated satellite observations and in situ measurements, Atmos. Chem. Phys., 18(15),
1240 11303–11322, doi:10.5194/acp-18-11303-2018, 2018.

Swap, R., Garstang, M., Greco, S., Talbot, R. and Kallberg, P.: Saharan dust in the Amazon Basin, Tellus, 44B(2), 133–149, 1992.

Tie, X. and Cao, J.: Aerosol pollution in China: Present and future impact on environment, Particuology, 7(6), 426–431, doi:10.1016/j.partic.2009.09.003, 2009.

1245 Uematsu, M., Duce, R. A. and Prospero, J. M.: Deposition of Atmospheric Mineral Particles in the North Pacific Ocean, J. Atmos. Chem., 3, 123–138, 1985.

Usher, C. R., Michel, A. E. and Grassian, V. H.: Reactions on Mineral Dust, Chem. Rev., 103(12), 4883–4939, doi:10.1021/cr020657y, 2003.

Wagenbach, D., Ducroz, F., Mulvaney, R., Keck, L., Minikin, A., Legrand, M., Hall, J. S. and Wolff, E. W.: Sea-salt aerosol
1250 in coastal Antarctic regions, J. Geophys. Res., 103(D9), 10,910-961,974, 1998.

Wang, P. K., Grover, S. N. and Pruppacher, H. R.: On the Effect of Electric Charges on the Scavenging of Aerosol Particles by Clouds and Small Raindrops, J. Atmos. Sci., 35(9), 1735–1743, doi:https://doi.org/10.1175/1520-0469(1978)035<1735:OTEOEC>2.0.CO;2, 1978.

Wang, R., Tao, S., Balkanski, Y., Ciais, P., Boucher, O., Liu, J., Piao, S., Shen, H., Vuolo, M. R., Valari, M., Chen, H.,

1255   Chen, Y., Cozic, A., Huang, Y., Li, B., Li, W., Shen, G., Wang, B. and Zhang, Y.: Exposure to ambient black carbon derived from a unique inventory and high-resolution model, Proc. Natl. Acad. Sci. U. S. A., 111(7), 2459–2463, doi:10.1073/pnas.1318763111, 2014.

Wang, Y., Chakrabarti, A. and Sorensen, C. M.: A light-scattering study of the scattering matrix elements of Arizona Road Dust, J. Quant. Spectrosc. Radiat. Transf., 163, 72–79, doi:10.1016/j.jqsrt.2015.05.002, 2015.

1260   Wolff, E., Fischer, H., Fundel, F., Ruth, U., Twarloh, B., Littot, G., Mulvaney, R., Rothlistberger, R., DeAngelis, M., Boutron, C., Hasson, M., Jonsell, U., Hutterli, M., Lambert, F., Kaufmann, P. R., Stauffer, B., Socker, T., Steffensen, J. P., Bigler, M., Siggard-Andersen, Udisti, R., Becagli, S., Castellano, E., Severi, M., Wagenbach, D., Barbante, C., Gabrielli, P. and Gaspari, V.: Southern Ocean sea-ice extent, productivity and iron flux over the past eight glacial cycles, Nature, 440, doi:10.1038/nature04614; 491--496, 2006.

1265   Wu, C., Lin, Z. and Liu, X.: Global dust cycle and uncertainty in CMIP5 models, Atmos. Chem. Phys. Discuss., 5, 1–52, doi:10.5194/acp-2020-179, 2020a.

Wu, M., Liu, X., Zhang, L., Wu, C., Lu, Z., Ma, P. L., Wang, H., Tilmes, S., Mahowald, N., Matsui, H. and Easter, R. C.: Impacts of Aerosol Dry Deposition on Black Carbon Spatial Distributions and Radiative Effects in the Community Atmosphere Model CAM5, J. Adv. Model. Earth Syst., 10(5), 1150–1171, doi:10.1029/2017MS001219, 2018.

1270   Wu, M., Liu, X., Yu, H., Wang, H., Shi, Y., Yang, K., Darmenov, A., Wu, C., Wang, Z., Luo, T., Feng, Y. and Ke, Z.: Understanding processes that control dust spatial distributions with global climate models and satellite observations, Atmos. Chem. Phys., 20(22), 13835–13855, doi:10.5194/acp-20-13835-2020, 2020b.

Yang, E. S., Gupta, P. and Christopher, S. A.: Net radiative effect of dust aerosols from satellite measurements over Sahara, Geophys. Res. Lett., 36(18), 1–5, doi:10.1029/2009GL039801, 2009.

1275   Yuan, H., Zhuang, G., Li, J., Wang, Z. and Li, J.: Mixing of mineral with pollution aerosols in dust season in Beijing: Revealed by source apportionment study, Atmos. Environ., 42(9), 2141–2157, doi:10.1016/j.atmosenv.2007.11.048, 2008.

Zender, C., Bian, H. and Newman, D.: Mineral Dust Entrainment and Deposition (DEAD) model: Description and 1990s dust climatology, J. Geophys. Res., 108(D14), 4416, doi:10.1029/2002JD002775, 2003.

Zhang, D., Iwasaka, Y., Matsuki, A., Ueno, K. and Matsuzaki, T.: Coarse and accumulation mode particles associated with

1280   Asian dust in southwestern Japan, Atmos. Environ., 40(7), 1205–1215, doi:10.1016/j.atmosenv.2005.10.037, 2006.

Zhang, J. and Christopher, S.: Long wave radiative forcing of Saharan dust aerosols estimated from MODIS, MISR and CERES observations on TERRA, Geophys. Res. Lett., 30(23), 2188, doi:10.1029/2003GL018479, 2003.

Zhang, L., Gong, S. L., Padro, J. and Barrie, L.: A size-segregated dry depositoin scheme for an atmospheric aerosol module, Atmos. Enviroment, 35, 549–560, doi:10.1016/S1352-2310(00)00326-5., 2001.

1285